1	The influence of terrain on the convective environment and associated convective
2	morphology from an idealized modeling perspective
3	
4	Submitted for publication as an ARTICLE in
5	Journal of the Atmospheric Sciences
6	Initial Manuscript Submitted: 18 July 2019
7	Revised Manuscript #1 Submitted: 17 January 2020
8	Revised Manuscript #2 Submitted: 14 April 2020
9	
10	
11	Jake P. Mulholland*, Stephen W. Nesbitt, Robert J. Trapp
12	Department of Atmospheric Sciences, University of Illinois at Urbana-Champaign,
13	Urbana, Illinois
14	
15	John M. Peters
16	Department of Meteorology, Naval Postgraduate School,
17	Monterey, CA
18 19 20 21 22 23 24 25	
26 27	*Corresponding author address: Jake P. Mulholland, Department of Meteorology, Naval Postgraduate School, 589 Dyer Road, Building 235, Monterey, CA, 93943-5114

Early Online Release: This preliminary version has been accepted for publication in *Journal of the Atmospheric Sciences*, may be fully cited, and has been assigned DOI 10.1175/JAS-D-19-0190.1. The final typeset copyedited article will replace the EOR at the above DOI when it is published.

E-mail: jake.mulholland@nps.edu

29 ABSTRACT

Orographic deep convection (DC) initiation and rapid evolution from supercells to mesoscale convective systems (MCS) are common near the Sierras de Córdoba, Argentina, which was the focal point of the Remote Sensing of Electrification, Lightning, And Mesoscale/microscale Processes with Adaptive Ground Observations (RELAMPAGO) field campaign. This study used an idealized numerical model with elongated north-south terrain similar to that of the Sierras de Córdoba to address how variations in terrain height affected the environment and convective morphology. Simulations used a thermodynamic profile from a RELAMPAGO event that featured both supercell and MCS storm modes. Results revealed that DC initiated earlier in simulations with higher terrain, owing both to stronger upslope flows and standing mountain waves. All simulations resulted in supercell formation, with higher terrain supercells initiating closer to the terrain peak and moving slower off the terrain. Higher terrain simulations displayed increases in both low-level and deep-layer wind shear along the eastern slopes of the terrain that were related to the enhanced upslope flows, supporting stronger and wider supercell updrafts/downdrafts and a wider swath of heavy rainfall. Deeper and stronger cold pools from these wider and stronger higher terrain supercells led to surging outflow that reduced convective available potential energy accessible to deep convective updrafts, resulting in quicker supercell demise off the terrain. Lower terrain supercells moved quickly off the terrain, merged with weaker convective cells, and resulted in a quasi-organized MCS. These results demonstrate that terrain-induced flow modification may lead to substantial local variations in convective morphology.

49

30

31

32

33

34

35

36

37

38

39

40

41

42

43

44

45

46

47

48

50

1. Introduction

Terrain can have profound impacts on the initiation, maturation, and decay of deep convection (DC). Insolation and subsequent heating of terrain surfaces relative to the cooler surrounding air hydrostatically lowers pressures, fostering anabatic upslope flows (e.g., Crook and Tucker 2005; Geerts et al. 2008). These upslope flows may converge near the terrain peak and result in the erosion of ambient convective inhibition (CIN), leading to cumulus, cumulus congestus, and in some instances, DC initiation (DCI). Terrain is also one of the leading instigators of mesoscale convective systems (MCSs; Zipser 1977) that can produce severe weather and heavy rainfall. In fact, climatological studies of MCSs show that a majority initiate in the lee of terrain over land (e.g., Velasco and Fritsch 1987; Laing and Fritsch 1997). Other modes of DC have also been observed to initiate and/or interact with terrain, such as supercells (e.g., Bluestein 2000; Bosart et al. 2006; Tang et al. 2016; Scheffknecht et al. 2017; Mulholland et al. 2018; Mulholland et al. 2019). Thus, it is clear that terrain exerts major influences on DCI through maturation and decay.

Numerous observational, modeling, and theoretical studies have advanced our understanding of how terrain impacts DCI (e.g., Orville 1965; Tucker and Crook 2005; Wilson and Roberts 2006; Kirshbaum 2011; Kirshbaum 2013; Kirshbaum and Wang 2014; and references therein) or how mature DC, such as supercells or MCSs, interact with terrain (e.g., Bosart et al. 2006; Frame and Markowski 2006; Letkewicz and Parker 2011; Markowski and Dotzek 2011; and references therein). While the impact of terrain on DCI is relatively straightforward to conceptualize and is thoroughly covered in the aforementioned literature, the impact of terrain on supercells and MCSs is a bit more nebulous. Observational studies of terrain influences on supercells, such as by Bosart et al. (2006) and Tang et al. (2016), showed evidence for localized

regions of enhanced low-level vertical wind shear (due to flow channeling) and larger convective available potential energy (CAPE) (due to moisture "pooling"), both of which were favorable for supercell sustenance/strengthening. Observational studies, however, can only be used to a certain extent to discuss the relative influence of terrain on DC. In other words, there is no way to know the true influences of terrain since we cannot (in reality) remove terrain and observe the outcome on DC and/or the environment. Thus, numerical models are often used to help address research questions related to terrain influences on DC (e.g., Markowski and Dotzek 2011).

75

76

77

78

79

80

81

82

83

84

85

86

87

88

89

90

91

92

93

94

95

96

Only a limited number of numerical modeling studies have attempted to address how terrain influences supercells and MCSs. Frame and Markowski (2006) and Letkewicz and Parker (2011) both used an idealized numerical modeling framework to study how terrain-crossing MCSs changed in intensity and structure following interactions with terrain. Markowski and Dotzek (2011) also used an idealized numerical modeling framework to analyze mature supercells crossing terrain. Comparatively few studies, however, have been conducted on the influence of terrain on the full evolution of DC, such as from DCI to supercell to MCS. Soderholm et al. (2014) analyzed convective storm morphology near the Black Hills, an isolated mountain range in South Dakota with a maximum terrain height ~2200 m. Using both a 10 yr observational climatology and idealized numerical modeling simulations, they found that orographically forced convective cells (within weak wind shear environments) were weaker off the terrain owing to greater CIN. In stronger wind shear environments, more organized and longer-lived MCS and supercellular convective modes were favored. Their major finding was that convective storm morphology was relatively insensitive to thermodynamic perturbations induced by terrain, but was more strongly modulated by wind shear perturbations induced by terrain.

Mulholland et al. (2019) provided a detailed case study of an orographic supercell-to-MCS transition event in Argentina, South America. In addition to an observational overview of the event, the authors conducted a series of Weather Research and Forecasting (WRF) model simulations in which the terrain of the Sierras de Córdoba was systematically raised or lowered between -40% to +40%, relative to the control terrain height peak of ~2500 m. Their results showed that higher terrain simulations had progressively earlier DCI owing to both enhanced standing mountain waves and stronger low-level upslope flows. Furthermore, when the terrain was raised (lowered), wind shear increased (decreased) and CAPE decreased (increased) relative to the control simulation. These environmental differences resulted in the fastest supercell-to-MCS upscale growth within the control simulation, with progressively slowed (non-existent) upscale growth in higher (lower) terrain height simulations. While Mulholland et al. (2019) showed modifications of the terrain influenced this particular event in a real-data model configuration (including mesoscale-to-synoptic scale influences, such as a low-level jet, front), we seek to test particular hypotheses in a more controlled model configuration to assess terrain-convective morphology interactions.

97

98

99

100

101

102

103

104

105

106

107

108

109

110

111

112

113

114

115

116

117

118

119

The discrepancies in just how strongly terrain impacts the full convective life cycle of DC motivates further research into this topic. Owing to the strong regulation of severe weather hazard type by parent convective mode (e.g., supercells = greater tornado/large hail threat; MCSs = greater damaging winds/flash flooding threat; Trapp et al. 2005; Dial et al. 2010; Smith et al. 2012), it is vitally important to understand how terrain may impact what convective mode(s) is (are) favored in a given environment. Our central research question is: How do terrain induced modifications to a given supercell/MCS background environment affect deep convective morphology? Our central hypothesis to this research question is: Terrain induced upslope flow, and the associated terrain

induced modifications to the vertical wind shear profile, are capable of strongly modulating the intensity of supercell updrafts, cold pool generation, and subsequently, the upscale evolution of supercells into an MCS. To address our hypothesis, an idealized numerical modeling framework is adopted in which an array of varying terrain height simulations (greater range of terrain heights than the aforementioned studies) are conducted for a given environment. The use of an idealized numerical modeling framework is chosen over a real-data modeling framework (as in Mulholland et al. 2019) given its ability to more "cleanly separate" the specific roles of terrain effects on the environment and subsequent convective morphology (i.e., remove mesoscale-to-synoptic scale influences, such as warm air advection, low-level jets, and fronts). A description of the experimental design is provided in section 2. Section 3 contains the results from the idealized numerical modeling simulations and related discussion, and conclusions are located in section 4.

2. Experimental design

a. Numerical modeling setup

A series of idealized numerical model simulations were conducted using Cloud Model 1 (CM1; Bryan and Fritsch 2002) version 19.7. CM1 is a compressible, nonhydrostatic numerical model. The CM1 simulations were conducted with a uniform horizontal grid spacing of 500 m and a uniform vertical grid spacing of 250 m over a domain with dimensions 324 x 504 x 20 km³ (648 x 1008 x 80 grid points). Sensitivity test simulations conducted with a uniform horizontal grid spacing of 250 m, a uniform vertical grid spacing 125 m, and a vertical dimension of 24 km for the 4500 m terrain configuration showed little difference in convective morphology¹, thus supporting the use of a relatively coarser resolution and shallower domain. The lower boundary

¹ Notable differences between 4500 m sensitivity tests: (1) DCI occurred slightly earlier in the higher resolution simulations, (2) more persistent DC in higher resolution simulations following the gust front surge, and (3) largest morphological differences late in the model integration.

condition was semi-slip with the surface exchange coefficient for momentum (C_D) based on Fairall et al. (2003) at low-to-mid wind speeds, and Donelan (2004) at higher wind speeds (the default option in CM1), while the (constant) surface exchange coefficient for enthalpy (C_E) was based on the specified land-use index. The top boundary condition was rigid and free slip. A Rayleigh damping layer (coefficient = 3.33 x 10^{-3} s⁻¹) was applied above 15 km to minimize the artifacts of the rigid top boundary.

To study the effects of terrain on convective morphology and the surrounding environment, seven different terrain configurations were implemented in the simulations. Terrain was specified as an elliptically shaped mountain that was stretched in the north-south direction to mimic the approximate shape and areal extent of the Sierras de Córdoba. The terrain height (Z_s) was modified from the function presented in Döernbrack et al. (2005) and was specified as:

152 (1)
$$Z_s(x,y) = h * \left[\left(1 + \left(\frac{x}{a} \right)^2 \right)^{-1.5} \right],$$

where h = halfwidth (2.5 km), a = 10 km, and a = 10 km

154 (2)
$$X = \sqrt{(x + \gamma x_{max})^2 + \beta [(\alpha y + \varphi y_{max})^2]},$$

where $\gamma = x$ -position center of terrain (0.65), $\varphi = y$ -position center of terrain (0.10), $\beta = \text{factor to}$ stretch entire terrain in north-south direction (0.15), $\alpha = \text{factor to}$ only stretch maximum terrain height in north-south direction (0.40), $x_{max} = \text{length of domain in } x$ -direction (324 km), and $y_{max} = \text{length of domain in } y$ -direction (504 km). Seven different terrain height peaks of 500 m, 1500 m, 2000 m, 2500 m (Control: CTRL), 3000 m, 3500 m, and 4500 m were implemented. An example plan view of the 2500m-CTRL terrain configuration and west-to-east oriented vertical cross sections through all terrain peaks for these variable settings is depicted in Fig. 1.

Radiation and surface fluxes of heat, moisture, and momentum were included to allow for the development of realistic slope flows and natural DCI *without* prescribing a warm/cold "bubble"

in proximity to the heated terrain. Longwave and shortwave radiation were parameterized using the RRTMG scheme (Iacono et al. 2008) derived from the WRF model. The initialization of the radiation scheme included the following specifications: 1200 UTC 25 January 2019 at 31.30°S and 64.21°W (time and location of where the input sounding was located; e.g., Fig. 2). The radiation scheme was called every 5 min. All horizontal lateral boundaries were periodic to allow for the diurnal evolution of the initial thermodynamic and wind profiles within the domain. Surface fluxes of heat, moisture, and momentum were parameterized using the Monin-Obukhov similarity theory surface layer model (Grell et al. 1994). The surface fluxes were dependent on the user specified land-use category, which in this study was "irrigated cropland" with a soil moisture availability of 0.5 (as in Nowotarski et al. 2014). Due to the coupled atmospheric radiation-landsurface models used in these simulations, grid translation (i.e., uniform wind subtracted from base state winds) was not possible, thus necessitating the relatively large domain size and coarser horizontal and vertical grid spacings. The two-moment Morrison microphysics package (Morrison et al. 2009) was used in all simulations with hail as the prognostic rimed ice hydrometeor species. The simulations used a time step of 3 s, were integrated for 8 h, and model output was saved every 5 min. Coriolis acceleration was turned on for a sensitivity test simulation for the 4500 m terrain configuration (latitude = 31.30° N and $f = 7.58 \times 10^{-5} \text{ s}^{-1}$). The results from this additional simulation (not shown) were qualitatively similar² to the simulation with Coriolis acceleration turned off, and thus, the rest of the simulations neglected Coriolis acceleration. A summary of the CM1 configuration is located in Table 1.

164

165

166

167

168

169

170

171

172

173

174

175

176

177

178

179

180

181

182

² Main difference between the 4500 m terrain height simulation with/without Coriolis acceleration: (1) supercell in the 4500m-Coriolis-ON simulation was slightly weaker and less organized than in the 4500m-Coriolis-OFF simulation.

The input thermodynamic profile for the CM1 simulations was derived from an observed sounding from the Ingeniero Aeronáutico Ambrosio L.V. Taravella International Airport in Córdoba, Argentina (World Meteorological Organization site code 87344), at 1200 UTC 25 January 2019 (Fig. 2) during the extended observing period of the Remote Sensing of Electrification, Lightning, And Mesoscale/microscale Processes with Adaptive Ground Observations (RELAMPAGO) field campaign. Colorado State University C-band radar (31.63°S, 64.17°W, elevation 421 m) deployed for RELAMPAGO observed a vertically intense orographic supercell that rapidly transitioned into an MCS (Fig. 3; also see Fig. S1), similar to the case study presented in Mulholland et al. (2019) and climatological upscale growth events documented in Mulholland et al. (2018). The sounding was characterized by a nocturnal near-surface inversion layer with a surface dewpoint temperature of 26°C and mixing ratio of 23 g kg⁻¹. This near-surface inversion layer was vertically mixed out in the simulations owing to the inclusion of radiative fluxes. The CAPE and CIN for an air parcel with properties averaged over the lowest 100 hPa (most unstable parcel) were $\sim 2900 \text{ J kg}^{-1}$ ($\sim 4781 \text{ J kg}^{-1}$) and $\sim -175 \text{ J kg}^{-1}$ ($\sim -110 \text{ J kg}^{-1}$), respectively. The mixed-layer lifting condensation level (LCL) was ~1030 m above ground level (AGL), level of free convection (LFC) ~2690 m AGL, and equilibrium level (EL) ~15000 m AGL. The input wind profile was based on the analytic quarter circle wind hodograph from Rotunno and Klemp (1982) (Fig. 2b). The observed wind profile from 1200 UTC 25 January 2019 was not used for the simulations as deep-layer wind shear magnitudes early on this day were sub-optimal for supercell formation, likely due to the proximity of the sounding site to the terrain (e.g., 0–6 km wind shear $^3 = \sim 10-15$ m s $^{-1}$; not shown). The wind shear vector veered with increasing height from southerly to westerly over the lowest 2 km and stayed westerly above. The initial near-surface

184

185

186

187

188

189

190

191

192

193

194

195

196

197

198

199

200

201

202

203

204

³ Wind shear throughout the article will refer to the bulk wind difference, calculated as a simple vector subtraction between the upper-level horizontal wind vector and the lower-level horizontal wind vector (units: m s⁻¹).

wind was approximately calm and did not contain any upslope component. To remain consistent with a large portion of the established severe convective storms literature, all simulations were based around a Northern Hemisphere-centric framework, i.e., a "right-moving" supercell (main focus of paper) was one that deviated to the right of the mean wind shear vector and rotated cyclonically (to avoid any confusion with the aforementioned Southern Hemisphere references).

The input wind hodograph captured the salient features accompanying orographic DC events in north central Argentina, such as sharp veering of winds with increasing height near the terrain peak, and a gradual increase in the magnitude of (approximately) westerly winds with increasing height (e.g., see Fig. 15 from Mulholland et al. 2018). Note that this background environment was dramatically different from the weaker wind shear/CAPE environment used to study DC morphology over the Black Hills in South Dakota by Soderholm et al. (2014). To facilitate the generation of a turbulence spectrum, random potential temperature perturbations, with a maximum amplitude of |0.5 K|, were introduced uniformly across the domain below 1 km in the initial conditions (e.g., Nowotarski et al. 2014; Peters et al. 2019a; Peters et al. 2020). DC in the simulations initiated owing to the inclusion of radiation and surface fluxes, which quickly led to upslope flows and subsequent low-level convergence, ascent, and erosion of ambient CIN (in line with upslope flow onset and evolution for the given terrain height, width, and areal extent, e.g., Egger et al. 2005; Zängl and Chico 2006; Geerts et al. 2008).

3. Results and discussion

All seven simulations resulted in DCI near the terrain, with higher terrain simulations displaying earlier DCI (Figs. 4 and 5–far left panels; Table 2; also see radar animation in Fig. S2). Lower terrain simulations resulted in DCI mainly along a low-level convergence zone to the north of the terrain peak (not shown) whereas the 2500 m-CTRL simulation and all higher terrain

simulations resulted in DCI mainly downwind (east) of the terrain peak. West-to-east oriented Hovmöller diagrams taken through the terrain peaks and calculated at 1000 m above the terrain peaks during the first 3 h of the simulations revealed that the 2500m-CTRL and all higher terrain simulations had a standing mountain wave that monotonically increased in strength with increasing terrain height (Fig. 6). A strengthening westerly flow component with increasing altitude impinged on the terrain peaks, resulting in stronger standing mountain waves in higher terrain simulations (Fig. 7). The upward and downward branches of these standing mountain waves, with maximum/minimum vertical velocities between -4 to 4 m s⁻¹, did not extend more than 25–50 km east of the terrain peaks for any of the terrain simulations (Figs. 6 and 7; also see animation in Fig. S3). An upward wave branch was located just downstream of the terrain peak in these higher terrain simulations, aiding in the earlier erosion of ambient CIN due to adiabatic cooling (color shading in Fig. 6). In addition to stronger standing mountain waves in higher terrain simulations, stronger heating of the elevated terrain and subsequent greater horizontal buoyancy and perturbation pressure gradients resulted in enhanced low-level upslope flow (Figs. 8 and 9). Time series of vertically averaged 0–1 km zonal wind that was then spatially averaged over a 50 x 200 km² box with the west-central side of the box centered ~50 km east of the terrain peaks revealed that the 4500m simulation displayed ~3–4 m s⁻¹ greater low-level upslope flow as compared to the 500m simulation (Fig. 9). Inflow soundings and hodographs derived from a grid point 25 x 25 km² to the south and east of the DCI locations at the time of DCI (i.e., first appearance of a lowest model level reflectivity ≥40 dBZ) for each simulation revealed minimal thermodynamic differences, but relatively larger wind profile differences, with higher terrain hodographs displaying a greater toward-terrain flow component in the lowest few kilometers (Fig. 10; e.g., greater south-southeasterly low-level flow). The combination of enhanced low-level upslope flow

229

230

231

232

233

234

235

236

237

238

239

240

241

242

243

244

245

246

247

248

249

250

convergence on the terrain peaks and the presence of a standing mountain wave explains the earlier DCI in higher terrain simulations and is in line with the results from the WRF terrain height simulations presented in Mulholland et al. (2019). Additional analysis of these terrain-induced environmental variations and their effect on subsequent storm evolution are discussed throughout the remainder of this section.

252

253

254

255

256

257

258

259

260

261

262

263

264

265

266

267

268

269

270

271

272

273

274

Remarkably, given the limiting assumptions of the idealized numerical modeling framework adopted here, the resultant convective evolution following DCI in the 2500 m-CTRL simulation resembled the convective evolution of the observed orographic supercell-to-MCS transition on 25 January 2019 (compare radar animations in Figs. S1 and S2). Simulations with terrain lower than the 2500m-CTRL generally displayed less organized DC with a tendency for clustering of weaker convective cells owing to cold pool mergers with an eventual transition toward a quasi-organized MCS (Fig. 11; also see animation in Fig. S4-top row). In contrast, a distinct change in the character of convective evolution was noted for all terrain simulations above the 2500m-CTRL, with relatively isolated, right-moving supercells nearer the terrain peaks (Fig. 12; also see animation in Fig. S4-bottom row). These higher terrain supercells did not interact nearly as much with the weaker surrounding convective cells as did the lower terrain supercells; instead, the mesocyclones of these supercells were essentially "undercut" by surging outflow associated with the supercell cold pools along both their forward and rear flanks (e.g., Fig. 12bottom row). Finley et al. (2001) depicted a similar process of surging cold outflow undercutting a supercell's mesocyclone in numerical simulations. This surging cold pool evolution is highlighted in south-to-north oriented vertical cross-sections taken through the maximum 2–5 km updraft helicity (UH_{MAX}) locations (along dotted black horizontal lines in Figs. 11 and 12) for each simulation (UH $_{MAX}$ at Y-distance = 0 km in Figs. 13 and 14). The higher-terrain supercell cold

pools were initially deeper and stronger, leading to southward-surging outflow away from the mesocyclones in these simulations (e.g., Fig. 14-bottom row; also see Fig. S5). The Pearson linear correlation coefficient (hereafter: CC) between maximum terrain height and minimum lowest model level potential temperature perturbation temporally averaged over the first 7 h of the simulations was -0.84, suggesting a robust relationship between maximum terrain height and the supercell average cold pool strengths (Fig. 15h). This surging outflow, and resultant increasing spatial separation between the deep convective updrafts associated with the supercell mesocyclones and their near-surface outflow boundaries, resulted in air parcels having to travel 25–50 km overtop the cold pool before entering deep convective updrafts (e.g., Fig. 14–bottom row; e.g., Peters and Schumacher 2016). As a result of this increased distance between near-surface outflow boundaries and their parent mesocyclones in higher terrain simulations, the magnitude of CAPE that reached the remaining deep convective updrafts was reduced (e.g., Fig. 14-bottom row). Once the higher terrain supercells began to grow upscale into an MCS via this process of southward-surging outflow, and CAPE was reduced, the resulting updrafts were comparatively weaker than their lower terrain counterparts and by the end of the simulations, only weaker DC cells developed well behind the supercell near-surface outflow boundaries (e.g., Fig. 12–T = 390 min; Fig. 14-T = 390 min).

275

276

277

278

279

280

281

282

283

284

285

286

287

288

289

290

291

292

293

294

295

296

Runtime accumulated swaths of UH depicted that higher terrain supercells were wider, more coherent, and had motions that deviated more to the right of the mean deep-layer wind shear (see red arrows⁴ in Fig. 15). Given that higher terrain supercells generally moved slower (i.e., more "anchored" to the terrain; see radar animation in Fig. S2) and more to the right of the deep-layer wind shear meant that they were influenced by terrain-induced perturbations (e.g., enhanced wind

⁴ The focus of the remainder of the article is on the right-moving supercells denoted by red arrows in Fig. 12 as these were most directly influenced by terrain modifications.

shear) for lengthier periods compared to their lower terrain supercell counterparts. Time series of 2–8 km updraft effective radii ($R_{up} = \sqrt{\frac{A}{\pi}}$, where A = area of the updraft, defined using the largest contiguous horizontal area of 2–8 km vertically averaged vertical velocity $\overline{w_{up}}$ exceeding 15 m s⁻¹) and 2–5 km mesocyclone effective radii R_{meso} (defined using the largest contiguous horizontal area of UH exceeding 250 m² s⁻²) confirmed that higher terrain supercell updrafts/mesocyclones were indeed wider than their lower terrain supercell updraft/mesocyclone counterparts (Fig. 16a-b). For example, the maximum R_{up} and R_{meso} for the 4500m supercell were 5.7 km and 4.8 km, respectively, while the maximum R_{up} and R_{meso} for the 500m supercell were 4.0 km and 2.1 km, respectively (Fig. 16a-b). The range of simulated supercell updraft effective radii depicted here generally fall within the range of simulated supercell updraft effective radii that resulted from variations in both low-level and deep-layer wind shear presented by Peters et al. (2019b). Robust linear relationships between maximum terrain height and maximum R_{up} and maximum R_{meso} were noted with CC values of 0.83 and 0.95, respectively (Fig. 16d-e).

In addition to being wider, higher terrain supercell updrafts were also stronger (Fig. 17a). Time series of both $\overline{w_{up}}$ and UH_{MAX} confirm that higher terrain supercells had stronger rotating updrafts compared to lower terrain supercells (Fig. 17a-b). Maximum $\overline{w_{up}}$ and UH_{MAX} for the 4500m supercell were 43.0 m s⁻¹ and 4701.9 m² s⁻², respectively, whereas the maximum $\overline{w_{up}}$ and UH_{MAX} for the 500m supercell were 26.9 m s⁻¹ and 916.6 m² s⁻², respectively (Fig. 17a-b). Strong linear relationships between maximum terrain height and both maximum $\overline{w_{up}}$ and maximum UH_{MAX} were found, with *CC* values of 0.94 and 0.89, respectively (Fig. 17c and 17e). Furthermore, higher terrain supercell downdrafts were also wider (Fig. 16c; R_{dn} , defined using largest contiguous horizontal area of 1–4 km vertically averaged vertical velocity $\overline{w_{dn}}$ less than -10 m s⁻¹

¹) and stronger (Fig. 17a). Maximum R_{dn} (minimum $\overline{w_{dn}}$) for the 4500m supercell was 2.8 km (-18.9 m s⁻¹), whereas maximum R_{dn} (minimum $\overline{w_{dn}}$) for the 500m supercell was 1.2 km (-17.6 m s⁻¹) (Figs. 16c and 17a). A strong linear relationship between maximum terrain height and maximum R_{dn} was manifest with a CC value of 0.84 (Fig. 16f), whereas a weaker linear relationship existed between maximum terrain height and minimum $\overline{w_{dn}}$ with a CC value of -0.53 (Fig. 17d). Similar to the idealized supercell simulations presented by Marion and Trapp (2019), these wider and stronger higher terrain supercell drafts directly led to a wider swath of heavy rainfall (Fig. 18). A corresponding strong linear relationship (CC = 0.85) was noted between maximum terrain height and maximum rainfall accumulation (Fig. 18h). Maximum rainfall accumulation for the 4500m supercell was 27.2 cm, whereas the maximum rainfall accumulation for the 500m supercell was 10.5 cm (Fig. 18). The heavier precipitation likely led to a greater contribution to negative buoyancy via condensate loading which fostered the stronger downdrafts and cold pools in higher terrain supercells (e.g., Fig. 15).

Next, all terrain simulation supercell updrafts were both subjectively and objectively tracked to characterize the near-storm, "inflow" environments. To objectively track updrafts, we first found the horizontal location (x_m, y_m) of column maximum vertical velocity (w_{MAX}) within the domain at a given time as a "first guess". We then subjectively compared the time series of x_m and y_m to the track of the most intense updraft within the domain, and removed points that were not associated with the right-moving supercell nearest terrain (e.g., see red arrows in Fig. 15a-g). We also discarded points when the domain w_{MAX} was <20 m s⁻¹. The final supercell track (x_s, y_s) was computed by applying a Gaussian filter with a temporal radius of influence of 30 min to x_m and y_m (after all non-right-moving supercell points had been removed). A second subjective visual analysis was then performed to affirm the correspondence of x_s and y_s with the most intense storm

in the domain (i.e., the right-moving supercell nearest terrain). The time series of storm motion vectors $\mathbf{C}(\mathbf{t}) = c_x \hat{\mathbf{i}} + c_y \hat{\mathbf{j}} = \frac{dx_s}{dt} \hat{\mathbf{i}} + \frac{dy_s}{dt} \hat{\mathbf{j}}$ was then computed using second order centered-intime finite differences.

To specifically assess quantities within the supercell "inflow" regions, we drew a 40 x 40 km² box (hereafter: inflow box⁵) at each time, with the north and west corner of the box positioned at x_s and y_s . The average depth of the effective inflow layer (EIL; calculated using the CAPE and CIN criteria from Thompson et al. 2007) from the input sounding was approximately 4.25 km. Given that the EIL flow generally entered deep convective updrafts from the south and east (not shown) justified our specific positioning of the inflow box. Quantities were vertically and/or horizontally averaged within the inflow box, with all points of w > 5 m s⁻¹ excluded from these averages to avoid updraft influences. For instance, storm-relative (SR) flow vectors were computed by first averaging u and v within the inflow box, and then subtracting the storm motion vector, C(t). To determine factors that influenced R_{up} , R_{meso} , and R_{dn} (e.g., Fig. 16), updraft intensity (e.g., Fig. 17), and subsequent downdraft production (e.g., Fig. 17), quantities, such as 0–2 km SR flow, 0–2 km wind shear, 0–6 km wind shear, most-unstable (MU)CAPE, and MUCIN, were computed within the inflow box and compared to the time series of R_{up} , R_{meso} , and R_{dn} (Fig. 16a-c).

Time series of inflow 0–2 km SR flow and 0–2 km wind shear showed general increases with increasing terrain height, especially the 0–2 km SR flow between 150–300 min into the simulations (solid lines in Fig. 19a-b). Owing to potential cold outflow influences evidenced by decreases in 0–2 km SR flow and increases in 0–2 km wind shear after 300 min into the simulations, regression analyses between the supercell inflow time series variables and maximum

⁵ Various inflow box sizes were tested with similar conclusions as the final 40 x 40 km² box chosen for this analysis.

terrain height from each simulation were calculated using the following method: the output time corresponding to the maximum R_{up} was determined, and a \pm 30 min window around this output time was chosen to calculate 60 min temporally averaged supercell inflow time series variables, which were then compared with maximum terrain height from each simulation. The average 0-2 km SR flow displayed a strong linear relationship with maximum terrain height with a CC value of 0.92 (Fig. 20a), whereas the average 0–2 km wind shear vs. maximum terrain height had a CC value of 0.69 (Fig. 20b). The average 0-2 km SR flow and 0-2 km wind shear for the 4500m supercell were 22.7 m s⁻¹ and 22.0 m s⁻¹, respectively, while the average 0–2 km SR flow and 0–2 km wind shear for the 500m supercell were 11.4 m s⁻¹ and 13.8 m s⁻¹, respectively (Fig. 20a-b). Consistent with the increases in low-level SR flow and wind shear with increasing terrain height, 0–6 km wind shear also showed increases with increasing terrain height (dashed lines in Fig. 19b) and the average 0-6 km wind shear correspondingly had a strong linear relationship with maximum terrain height (CC = 0.94; Fig. 20c). The average 0–6 km wind shear for the 4500m supercell was 41.7 m s⁻¹, while the average 0–6 wind shear for the 500m supercell was 26.4 m s⁻¹ (Fig. 20c). These variations in low-level SR flow/wind shear and deep-layer wind shear span a similar parameter space presented in the idealized supercell simulations of Trapp et al. (2017), Marion and Trapp (2019), and Peters et al. (2019b). The stronger wind shear environment was consistent with the trend for wider (e.g., Fig. 16a-c) and stronger (e.g., Fig. 17a) supercell drafts in higher terrain simulations. In contrast, time series of MUCAPE and MUCIN generally showed weaker magnitudes of MUCAPE in higher terrain supercell inflow and comparable magnitudes of MUCIN within all supercell inflow (Fig. 19c-d). A strong negative correlation between average MUCAPE and maximum terrain height was noted, with a CC value of -0.90 (Fig. 20d), whereas no linear relationship was found between average MUCIN and maximum terrain height (CC = -

364

365

366

367

368

369

370

371

372

373

374

375

376

377

378

379

380

381

382

383

384

385

0.11; Fig. 20e). The average MUCAPE (MUCIN) for the 4500m supercell was 4194.7 J kg⁻¹ (-0.0 J kg⁻¹) while the average MUCAPE (MUCIN) for the 500m supercell was 5050.0 J kg⁻¹ (-0.0 J kg⁻¹) (Fig. 20d-e). These average values in MUCAPE are larger than previous idealized simulations of supercells, whereas the range in terrain-altered MUCAPE (500–1000 J kg⁻¹) shown here are similar to previous idealized supercell simulations that varied the base state MUCAPE (e.g., Kirkpatrick et al. 2011; Marion and Trapp 2019; Peters et al. 2019b). This means that even though higher terrain supercell updrafts were ingesting 500–1000 J kg⁻¹ less average MUCAPE as compared to lower terrain supercell updrafts, their updrafts were still wider and stronger owing to the stronger wind shear in their environments (e.g., Marion and Trapp 2019; Peters et al. 2019b).

To ensure that these essential inflow variations in wind shear were truly linked to terrain-induced modifications and not purely storm-induced modifications, low-level perturbation winds from the initial base state were calculated. Horizontal winds at the lowest model level in the initial base state were subtracted from horizontal winds at the lowest model level averaged between 3–4 h into the simulations (i.e., time frame leading up to supercell formation in most simulations). The results showed that while enhancements in low-level winds did occur within the inflow region of the higher terrain supercells, a vaster south-to-north enhancement was located along the eastern slopes of the terrain, south of the right-moving supercells (e.g., Fig. 21e-g). This narrow "ribbon" of enhanced low-level winds (5–10 m s⁻¹ stronger for higher terrain simulations) along the eastern slopes of the terrain is reminiscent of the low-level wind shear enhancements noted along the eastern slopes of the Sierras de Córdoba by Mulholland et al. (2019). This low-level wind shear enhancement was tied to the stronger low-level upslope flows noted in higher terrain simulations (e.g., Figs. 9 and 10).

The greater magnitudes of wind shear within the inflow region of the higher terrain supercells, both over shallow and deep layers, likely fostered the wider and stronger updrafts and downdrafts, in line with several recent papers relating wind shear to supercell draft properties (e.g., Dennis and Kumjian 2017; Trapp et al. 2017; Warren et al. 2017; Marion and Trapp 2019; Peters et al. 2019b). For example, Marion and Trapp (2019) showed that supercells in environments with stronger low- and deep-layer wind shear had resultant wider updrafts, wider downdrafts, deeper cold pools, and greater rainfall production. Furthermore, Peters et al. (2019b; 2020) showed that wider supercell updrafts in environments with stronger wind shear allowed them to be more resistant to entrainment-driven dilution, and thus, realize more of their core buoyancy, resulting in stronger upward vertical velocities. Enhanced upward dynamic forcing owing to the stronger deep-layer wind shear in the higher terrain supercell inflow may have also resulted in the stronger upward vertical velocities, especially in the low-to-midlevels (e.g., Weisman and Rotunno 2000; Peters et al. 2019b).

Overall, these results suggest that terrain-induced variations to vertical wind profiles were mainly responsible for the differences noted in convective morphology as compared to terrain induced thermodynamic variations, in line with conclusions drawn by Soderholm et al. (2014). Given that the higher terrain supercells generally moved slower than lower terrain supercells, and were located nearer the terrain peaks, they were more strongly affected by the aforementioned terrain-induced perturbations to the base state environment (e.g., enhanced wind shear). Lower terrain supercells moved off the terrain at a quicker pace, and correspondingly were influenced by weaker terrain-induced perturbations to CAPE/CIN and wind shear (i.e., the lower terrain supercell inflow more closely matched the quasi-homogenous environment off the terrain).

4. Conclusions

This study addressed the influences of terrain on the environment and resulting convective morphology using an idealized numerical modeling framework. Our objective was to analyze the full convective evolution, from DCI to supercell to MCS, in relation to a wide array of terrain heights (greater range of terrain heights than previous authors used). Seven idealized numerical modeling simulations were conducted in which the north-south model terrain (mimicking the Sierras de Córdoba in Argentina, South America) was altered by systematically varying maximum terrain height between 500 m and 4500 m.

432

433

434

435

436

437

438

439

440

441

442

443

444

445

446

447

448

449

450

451

452

453

The idealized numerical modeling simulations displayed systematic variations in DCI timing and location, as well as subsequent supercell intensity, updraft and downdraft structure, cold pool and rainfall characteristics, and upscale growth rates that varied with modified environmental characteristics caused by the simulations' terrain modifications. Similar to WRF simulations of an orographic supercell-to-MCS transition case study presented in Mulholland et al. (2019), the higher terrain simulations conducted here displayed earlier DCI. Such earlier DCI was attributed to earlier and stronger low-level upslope flows, along with dynamically enhanced upward vertical motions owing to a standing mountain wave. The stronger upslope flows also enhanced wind shear along the immediate eastern slopes of the terrain, and the enhanced wind shear (both low-level and deep-layer) fostered wider supercell updrafts with stronger vertical velocities. Supercell updraft width has been shown to scale with wind shear magnitude, with stronger wind shear leading to wider updrafts (e.g., Dennis and Kumjian 2017; Trapp et al. 2017; Warren et al. 2017; Marion and Trapp 2019; Peters et al. 2019b; Peters et al. 2020). These aforementioned studies used a more highly idealized numerical modeling framework (i.e., warm "bubble" initiation, no friction/radiation/fluxes/terrain), so the results shown here from a more

"realistic" setting further support the claim that stronger wind shear leads to wider supercell updrafts.

The wider and stronger updrafts also supported stronger/wider downdrafts and a wider area of heavy rainfall accumulation. The stronger and wider higher-terrain supercell downdrafts produced slightly deeper and relatively stronger cold pools, especially early in their convective morphology. Interestingly, the initially deeper higher-terrain supercell cold pools surged southward away from the parent DC, which reduced CAPE accessible to deep convective updrafts and led to a quicker demise of the nascent MCS (similar morphology also noted in Finley et al. 2001 and Klimowski et al. 2004). Perhaps the terrain blocked the higher terrain supercell cold pools, leading to an accumulation of negatively buoyant air and a resultant horizontal acceleration of the cold pool away from the parent DC (e.g., Xu et al. 2012; Phadtare 2018; Yin et al. 2020). Future work should seek to isolate this proposed cold pool blocking mechanism using modifications to the idealized numerical modeling framework used herein.

In summary, terrain-induced enhancements to wind shear over different tropospheric layers in close proximity to the terrain appeared more crucial to orographic DC morphology than terrain-induced alterations to the thermodynamic environment, in line with conclusions drawn by Soderholm et al. (2014). Even given the decreased MUCAPE within the inflow region of higher terrain supercell updrafts, the enhanced wind shear led to wider/stronger supercell updrafts with wider/stronger downdrafts and slightly deeper/stronger cold pools. There does appear to be some "tipping point" between the lower and higher terrain simulations, in context of the 2500m-CTRL simulation, as configured herein. The DC evolution between these two groups of simulations was rather different with the 2500 m-CTRL and all higher terrain simulations resulting an isolated orographic supercell that grew upscale into a short-lived MCS; whereas, the lower terrain

simulations depicted merging of weaker convective cells with the main supercell farther away from the terrain to form a longer-lasting MCS. The higher terrain supercells moved off the terrain at a slower pace, allowing them to be affected by the terrain-enhanced wind shear for lengthier periods. Thus, there might be some "optimal" terrain height for a specific convective morphology pathway, although such an optimal height would likely depend on environmental characteristics such as mixed-layer depth, depth of the vertically sheared layer, CAPE/CIN, among other pertinent atmospheric variables.

While the conclusions drawn here may be applicable to the environment common to the Sierras de Córdoba, how would DC behave in other environments (i.e., weaker CAPE, stronger wind shear) and terrain configurations (i.e., such as near the Rocky Mountains in the United States)? In the present study, we used a singular input sounding that was characterized by both large magnitudes of CAPE and vertical wind shear, and analyzed terrain-induced environmental variations on the supercell-to-MCS transition deep convective pathway. Future idealized numerical modeling simulations should include variations to the background CAPE and vertical wind shear environment, terrain configurations, and deep convective pathways, to test the robustness of the results presented herein. Finally, the idealized numerical modeling framework adopted here excludes the influences of baroclinic boundaries, low-level jets, upper-level troughs, among other synoptically relevant features that undoubtedly have an influence on convective morphology (e.g., Bunkers et al. 2006; Coniglio et al. 2010; Dial et al. 2010).

Acknowledgments

We are indebted to George Bryan for his creation, development, and support of CM1. The authors would like to thank the Servicio Meteorológico Nacional, Argentina, for their efforts during RELAMPAGO. The first author would like to thank Chuan-Chieh Chang, Geoffrey Marion, Benjamin Vega-Westhoff, Tzu-shun Lin, Itinderjot Singh, and Kevin Gray for computing assistance and Robert Rauber, Deanna Hence, Hugh Morrison, Christopher Nowotarski, Jana Houser, Bowen Pan, Bruno Ribeiro, and Janice Mulholland for many thought-provoking and fruitful discussions. The authors would like to thank the main editor, Louis Wicker, and three anonymous reviewers for their constructive reviews that greatly improved the manuscript. Computational resources were provided by the Computational and Information Systems Lab at the National Center for Atmospheric Research and the University of Illinois at Urbana-Champaign Keeling supercomputing cluster. Support for this work was made possible by National Science Foundation Grants AGS-1661799 for the first and second authors and AGS-1661800 for the third author.

523	References
524	Bluestein, H. B., 2000: A tornadic supercell over elevated, complex terrain: The Divide, Colorado,
525	storm of 12 July 1996. Mon. Wea. Rev., 128, 795–809.
526	
527	Bosart, L. F., A. Seimon, K. D. LaPenta, and M. J. Dickinson, 2006: Supercell tornadogenesis over
528	complex terrain: The Great Barrington, Massachusetts, tornado on 29 May 1995. Wea.
529	Forecasting, 21, 897–922.
530	
531	Bunkers, M. J., B. A. Klimowski, R. L. Thompson, and M. L. Weisman, 2000: Predicting supercell
532	motion using a new hodograph technique. Wea. Forecasting, 15, 61–79.
533	
534	—, J. S. Johnson, L. J. Czepyha, J. M. Grzywacz, B. A. Klimowski, and M. R. Hjelmfelt, 2006:
535	An observational examination of long-lived supercells. Part II: Environmental conditions and
536	forecasting. Wea. Forecasting, 21, 689–714.
537	
538	Bryan, G. H., and M. J. Fritsch, 2002: A benchmark simulation for moist nonhydrostatic numerical
539	models. Mon. Wea. Rev., 130, 2917–2928.
540	
541	Coniglio, M. C., J. Y. Hwang, and D. J. Stensrud, 2010: Environmental factors in the upscale
542	growth and longevity of MCSs derived from Rapid Update Cycle analyses. Mon. Wea. Rev., 138,
543	3514–3539.

- Crook, N. A., and D. F. Tucker, 2005: Flow over heated terrain. Part I: Linear theory and idealized numerical simulations. *Mon. Wea. Rev.*, **133**, 2552–2564.

 Dennis, E. J., and M. R. Kumjian, 2017: The impact of vertical wind shear on hail growth in simulated supercells. *J. Atmos. Sci.*, **74**, 641–663.
- Dial, G. L., J. P. Racy, and R. L. Thompson, 2010: Short-term convective mode evolution along
 synoptic boundaries. *Wea. Forecasting*, 25, 1430–1446.

553

557

560

563

- Donelan, M. A., B. K. Haus, N. Reul, W. J. Plant, M. Stiassnie, H. C. Graber, O. B. Brown, and
 E. S. Saltzman, 2004: On the limiting aerodynamic roughness of the ocean in very strong winds. *Geophys. Res. Lett.*, 31, L18306.
- Dörnbrack, A., J. D. Doyle, T. P. Lane, R. D. Sharman, and P. K. Smolarkiewicz, 2005: On physical reliability and uncertainty of numerical solutions. *Atmos. Sci. Lett.*, **6**, 118–122.
- Egger, J., and Coauthors, 2005: Diurnal circulation of the Bolivian Altiplano. Part I: Observations.
 Mon. Wea. Rev., 133, 911–924.
- Fairall, C. W., E. F. Bradley, J. E. Hare, A. A. Grachev, and J. B. Edson, 2003: Bulk parameterization of air—sea fluxes: Updates and verification for the COARE algorithm. *J. Climate*, 16, 571–591.

- 568 Finley, C. A., W. R. Cotton, and R. A. Pielke Sr., 2001: Numerical simulation of tornadogenesis 569 in a high-precipitation supercell. Part I: Storm evolution and transition into a bow echo. J. Atmos. 570 Sci., **58**, 1597–1629. 571 572 Frame, J., and P. Markowski, 2006: The interaction of simulated squall lines with idealized 573 mountain ridges. Mon. Wea. Rev., 134, 1919–1941. 574 575 Geerts, B., Q. Miao, and J. C. Demko, 2008: Pressure perturbations and upslope flow over a heated, 576 isolated mountain. Mon. Wea. Rev., 136, 4272–4288. 577 Grell, G. A., J. Dudhia, and D. R. Stauffer, 1994: A description of the fifth-generation Penn 578 579 State/NCAR Mesoscale Model (MM5). NCAR Tech. Note NCAR/TN-3981STR, 121 pp. 580 581 Iacono, M. J., J. S. Delamere, E. J. Mlawer, M. W. Shephard, S. A. Clough, and W. D. Collins, 582 2008: Radiative forcing by long-lived greenhouse gases: Calculations with the AER radiative transfer models. J. Geophys. Res., 113, D13103. 583 584 585 Kirkpatrick, C., E.W. McCaul, and C. Cohen, 2011: Sensitivities of simulated convective storms
- Kirshbaum, D. J., 2011: Cloud-resolving simulations of deep convection over a heated mountain.

to environmental CAPE. Mon. Wea. Rev., 139, 3514-3532.

589 *J. Atmos. Sci.*, **68**, 361–378.

586

587

591	—, 2013: On thermally forced circulations over heated terrain. J. Atmos. Sci., 70, 1690–1709.	
592		
593	—, and CC. Wang, 2014: Boundary-layer updrafts driven by airflow over heated terrain. J.	
594	Atmos. Sci., 71, 1425–1442.	
595		
596	Klimowski, B. A., M. R. Hjelmfelt, and M. J. Bunkers, 2004: Radar observations of the ea	
597	evolution of bow echoes. Wea. Forecasting, 19, 727–734.	
598		
599	Laing, A. G., and J. M. Fritsch, 1997: The global population of mesoscale convective complexes.	
600	Quart. J. Roy. Meteor. Soc., 123, 389–405.	
601		
602	Letkewicz, C. E., and M. D. Parker, 2011: Impact of environmental variations on simulated squall	
603	lines interacting with terrain. Mon. Wea. Rev., 139, 3163–3183.	
604		
605	Marion, G. R., and Trapp, R. J., 2019: The dynamical coupling of convective updrafts, downdrafts,	
606	and cold pools in simulated supercell thunderstorms. J. Geophys. Res., 124, 1–20.	
607		
608	Markowski, P. M., and N. Dotzek, 2011: A numerical study of the effects of orography on	
609	supercells. Atmos. Res., 100, 457–478.	
610		
611	Morrison, H., G. Thompson, and V. Tatarskii, 2009: Impact of cloud microphysics on the	
612	development of trailing stratiform precipitation in a simulated squall line: Comparison of one- and	
613	two-moment schemes. Mon. Wea. Rev., 137, 991–1007.	

614			
615	Mulholland, J. P., S. W. Nesbitt, R. J. Trapp, K. L. Rasmussen, and P. V. Salio, 2018: Convective		
616	storm life cycle and environments near the Sierras de Córdoba, Argentina. Mon. Wea. Rev., 146,		
617	2541–2557.		
618			
619	-, S. W. Nesbitt, R. J. Trapp, 2019: A case study of terrain influences on upscale convective		
620	growth of a supercell. Mon. Wea. Rev., Mon. Wea. Rev., 147, 4305-4324.		
621			
622	Nowotarski, C. J., P. M. Markowski, Y. P. Richardson, and G. H. Bryan, 2014: Properties of a		
623	simulated convective boundary layer in an idealized supercell thunderstorm environment. Mon.		
624	Wea. Rev., 142 , 3955–3976.		
625			
626	Orville, H. D., 1965: A numerical study of the initiation of cumulus clouds over mountainous		
627	terrain. J. Atmos. Sci., 22, 684–699.		
628			
629	Peters, J. M., and R. S. Schumacher, 2016: Dynamics governing a simulated mesoscale convective		
630	system with a training convective line. J. Atmos. Sci., 73, 2643–2664.		
631			
632	—, W. Hannah, and H. Morrison, 2019a: The influence of vertical wind shear on moist thermals. J.		
633	Atmos. Sci., 76, 1645–1659.		
634			
635	-, C. J. Nowotarski, and H. Morrison, 2019b: The role of vertical wind shear in modulating		

maximum supercell updraft velocities. J. Atmos. Sci., 76, 3169–3189.

637	
638	, C.J. Nowotarski, and G.L. Mullendore, 2020: Are supercells resistant to entrainment because
639	of their rotation?. J. Atmos. Sci., 77, 1475–1495.
640	
641	Phadtare, J., 2018: Role of Eastern Ghats orography and cold pool in an extreme rainfall event
642	over Chennai on 1 December 2015. Mon. Wea. Rev., 146, 943-965.
643	
644	Potvin, C. K., K. L. Elmore, and S. J. Weiss, 2010: Assessing the impacts of proximity sounding
645	criteria on the climatology of significant tornado environments. Wea. Forecasting, 25, 921–930.
646	
647	Rotunno, R., J., and J. B. Klemp, 1982: The influence of the shear-induced pressure gradient on
648	thunderstorm motion. Mon. Wea. Rev., 110, 136–151.
649	
650	Scheffknecht, P., S. Serafin, and V. Grubisic, 2017: A long-lived supercell over mountainous
651	terrain. Quart. J. Roy. Meteor. Soc., 143, 2973-2986.
652	
653	Smith, B. T., R. L. Thompson, J. S. Grams, C. Broyles, and H. E. Brooks, 2012: Convective modes
654	for significant severe thunderstorms in the contiguous United States. Part I: Storm classification
655	and climatology. Wea. Forecasting, 27, 1114–1135.
656	
657	Soderholm, B., B. Ronalds, and D. J. Kirshbaum, 2014: The evolution of convective storms
658	initiated by an isolated mountain ridge. Mon. Wea. Rev., 142, 1430–1451.

- Tang, B., M. Vaughn, R. Lazear, K. Corbosiero, L. Bosart, T. Wasula, I. Lee, and K. Lipton, 2016:
- Topographic and boundary influences on the 22 May 2014 Duanesburg, New York, tornadic
- 662 supercell. *Wea. Forecasting*, **31**, 107–127.

- Thompson, R. L., C. M. Mead, and R. Edwards, 2007: Effective storm-relative helicity and bulk
- shear in supercell thunderstorm environments. Wea. Forecasting, 22, 102–115.

666

- Trapp, R. J., S. A. Tessendorf, E. S. Godfrey, and H. E. Brooks, 2005: Tornadoes from squall lines
- and bow echoes. Part I: Climatological distribution. Wea. Forecasting, 20, 23–34.

669

- 670 —, G. R. Marion, and S. W. Nesbitt, 2017: The regulation of tornado intensity by updraft width.
- 671 *J. Atmos. Sci.*, **74**, 4199–4211.

672

- Tucker, D. F., and N. A. Crook, 2005: Flow over heated terrain. Part II: Generation of convective
- 674 precipitation. *Mon. Wea. Rev.*, **133**, 2565–2582.

675

- Velasco, I., and J. M. Fritsch, 1987: Mesoscale convective complexes in the Americas. *J. Geophys.*
- 677 *Res.*, **92**, 9591–9613.

678

- Warren, R. A., H. Richter, H. A. Ramsay, S. T. Siems, and M. J. Manton, 2017: Impact of
- variations in upper-level shear on simulated supercells. *Mon. Wea. Rev.*, **145**, 2659–2681.

682	Weisman, M. L., and R. Rotunno, 2000: The use of vertical wind shear versus helicity in
683	interpreting supercell dynamics. J. Atmos. Sci., 57, 1452–1472.
684	
685	Wilson, J. W., and R. D. Roberts, 2006: Summary of convective storm initiation and evolution
686	during IHOP: Observational and modeling perspective. Mon. Wea. Rev., 134, 23-47.
687	
688	Xu, W., E. J. Zipser, YL. Chen, C. Liu, YC. Liou, WC. H. Lee, and B. JD. Jou, 2012: An
689	orography-associated extreme rainfall event during TiMREX: Initiation, storm evolution, and
690	maintenance. Mon. Wea. Rev., 140, 2555–2574.
691	
692	Yin, J., D. Zhang, Y. Luo, and R. Ma, 2020: On the Extreme Rainfall Event of 7 May 2017 Over
693	the Coastal City of Guangzhou. Part I: Impacts of Urbanization and Orography. Mon. Wea. Rev.,
694	148 , 955–979.
695	
696	Zängl, G., and S. G. Chico, 2006: The thermal circulation of a grand plateau: Sensitivity to the
697	height, width, and shape of the plateau. Mon. Wea. Rev., 134, 2581–2600.
698	
699	Zipser, E. J., 1977: Mesoscale and convective-scale downdrafts as distinct components of squall-
700	line circulation. Mon. Wea. Rev., 105, 1568–1589.
701	
702	
703	

705 Tables and Figures

706

Table 1. Summary table of the CM1 configuration.

Attribute	Value / setting
Fully compressible	yes
Horizontal grid spacing	500 m
Vertical grid spacing	250 m
Vertical coordinate	height (m)
Number of x, y, z grid points	648 x 1008 x 80
Top (bottom) LBC*	free slip (semi-slip)
North and south LBC*	periodic
East and west LBC*	periodic periodic
Microphysics	height (m) 648 x 1008 x 80 free slip (semi-slip) periodic periodic Morrison two moment; Morrison et al. (2009) 6th order Turbulent Kinetic Energy yes yes 75 m² s⁻¹ and 0.04 RRTMG scheme; Iacono et al. (2008) Monin-Obukhov; Grell et al. (1994)
Diffusion	6 th order
Subgrid turbulence	Turbulent Kinetic Energy
Rayleigh damping	yes 90.14
Dissipative heating	yes yes
2 nd and 6 th order diff. coef.	$75 \text{ m}^2 \text{ s}^{-1} \text{ and } 0.04$
Longwave/shortwave radiation	RRTMG scheme; Iacono et al. (2008)
Surface layer	Monin-Obukhov; Grell et al. (1994)
Land use index	Irrigated cropland; Soil moisture availability = 0.5 \(\)
Coriolis acceleration	off
Boundary layer physics	none
Cumulus parameterization	none

^{*}LBC -- lateral boundary condition

Table 2. Summary table of the number of minutes into the simulations of convection initiation (defined as the first appearance of lowest model level reflectivity \geq 40 dBZ).

Simulation	Convection Initiation
500 m	160*
1500 m	110*
2000 m	100*
2500 m-CTRL	95
3000 m	95
3500 m	75
4500 m	65

^{* –} mechanism for convection initiation was a low-level convergence zone to the north of the terrain peak (i.e., not directly near/over the terrain peak)

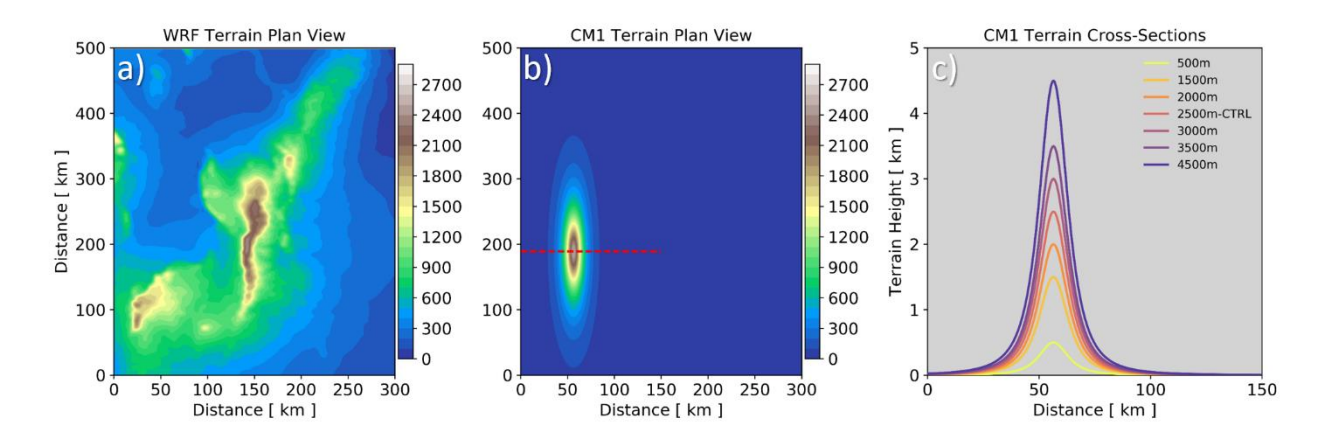


Fig. 1. (a) Plan view of terrain height (m) from a 1-km WRF simulation (adapted from Mulholland et al. 2019), (b) plan view of terrain height (m) from the 2500m-CTRL CM1 simulation and line along which the west-to-east oriented vertical cross sections of terrain are shown in panel c (red dashed line), and (c) west-to-east oriented vertical cross sections of terrain height taken through the peak of the terrain for each simulation (km; see red dashed line in panel b).

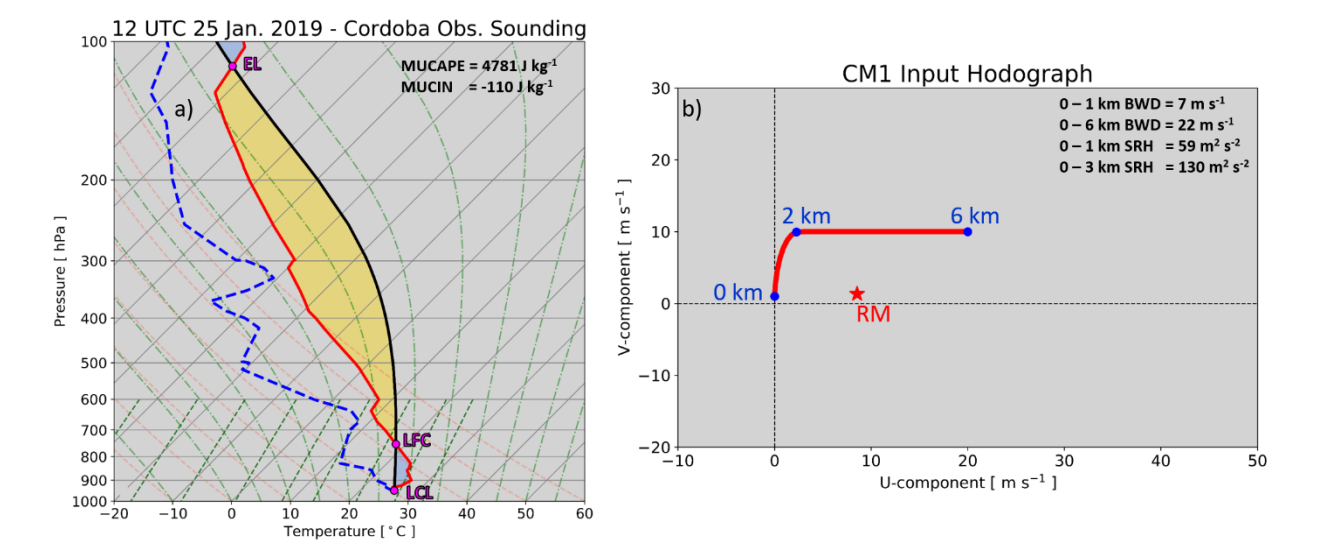


Fig. 2. Initial background state of the CM1 simulations. (a) 1200 UTC 25 January 2019 Ingeniero Aeronáutico Ambrosio L.V. Taravella International Airport in Córdoba, Argentina, sounding plotted on a skew-T log-P diagram. The red solid line is the air temperature (°C), the blue dashed line is the dewpoint temperature (°C), and the black solid line is the vertical path of a parcel lifted from the surface and (b) modified quarter-circle wind hodograph (from Rotunno and Klemp 1982) with the u-component of the wind on the x-axis (m s⁻¹) and the v-component of the wind on the y-axis (m s⁻¹). Acronyms defined: BWD = bulk wind difference, EL = equilibrium level, LCL = lifting condensation level, LFC = level of free convection, MUCAPE = most unstable convective available potential energy, MUCIN = most unstable convective inhibition, RM = right-moving supercell storm motion based upon Bunkers et al. (2000), and SRH = storm-relative helicity.

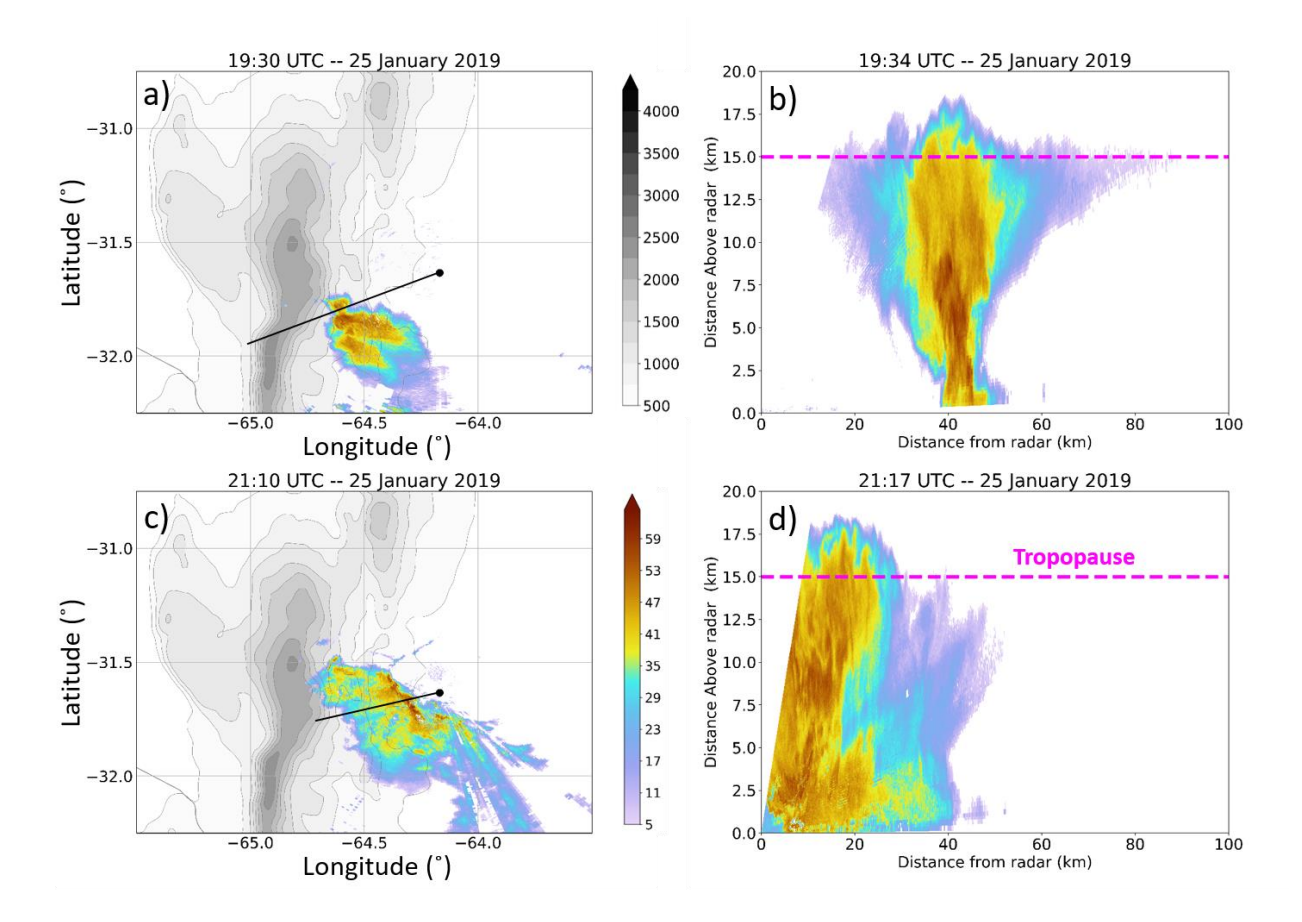


Fig. 3. Colorado State University C-band radar (black dot) data, showing (a) 19:30 UTC 25 January 2019 0.8° plan position indicator scan of radar reflectivity (dBZ) and terrain height (shaded and contoured in grey), (b) 19:34 UTC 25 January 2019 range height indicator scan of radar reflectivity (dBZ), (c) 21:10 UTC 25 January 2019 1.5° plan position indicator scan of radar reflectivity (dBZ) and terrain height (shaded and contoured in grey), and (d) 21:17 UTC 25 January 2019 range height indicator scan of radar reflectivity (dBZ). Note that the azimuths along which the range height indicator scans depicted in panels b and d are taken along are shown as thin black horizontal lines in panel a and c. The approximate tropopause height (based upon observed sounding shown in Fig. 2a) is marked by the horizontal dashed magenta line in panels b and d.

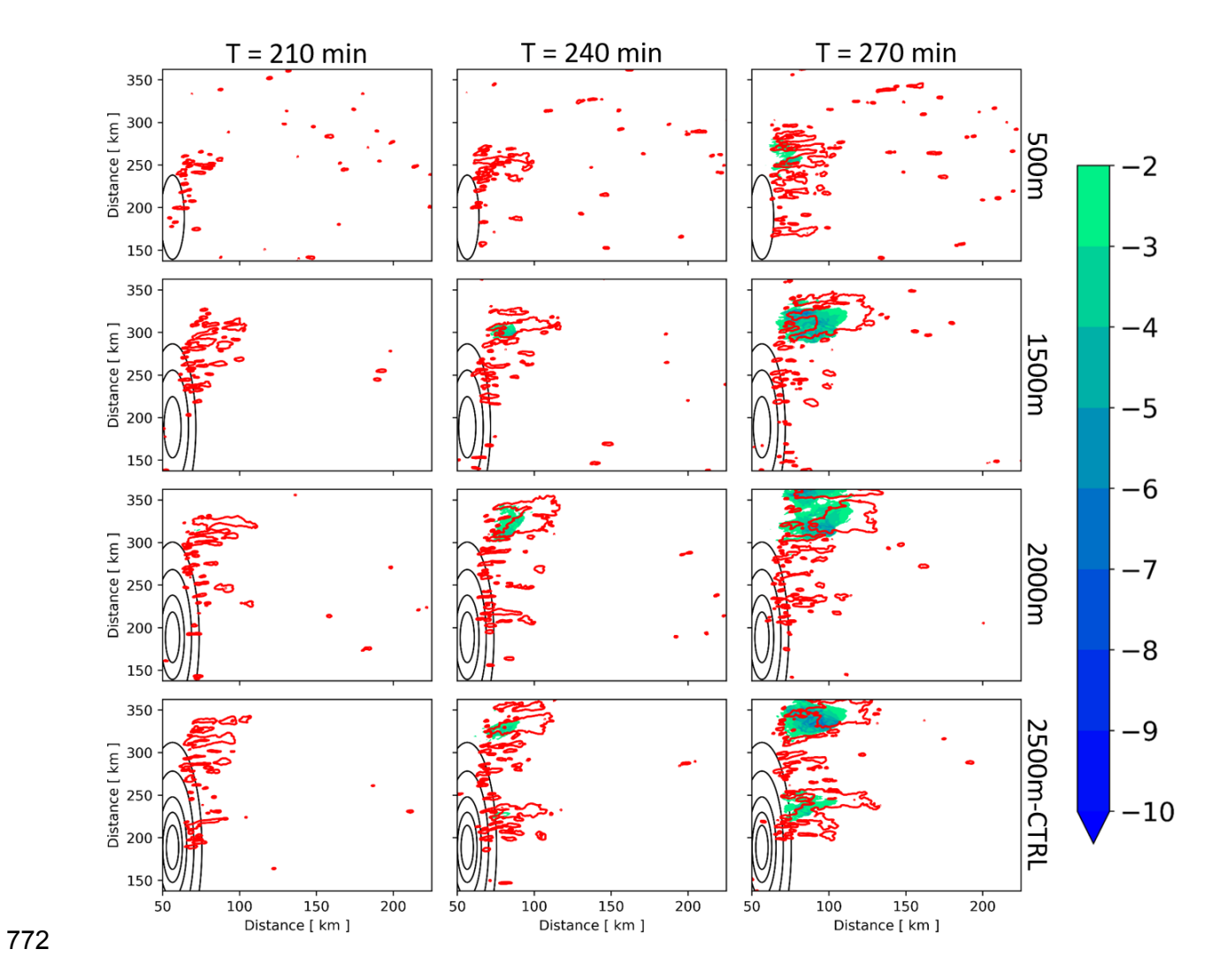


Fig. 4. Plan views of lowest model level reflectivity (red contour = 40 dBZ), lowest model level potential temperature perturbation (shaded; K), and terrain height (black contours = 250 m, 500 m, and 500 m increments thereafter). Rows = specific terrain simulation; Columns = output time (every 30 min). Note that only a portion of the full domain is shown.

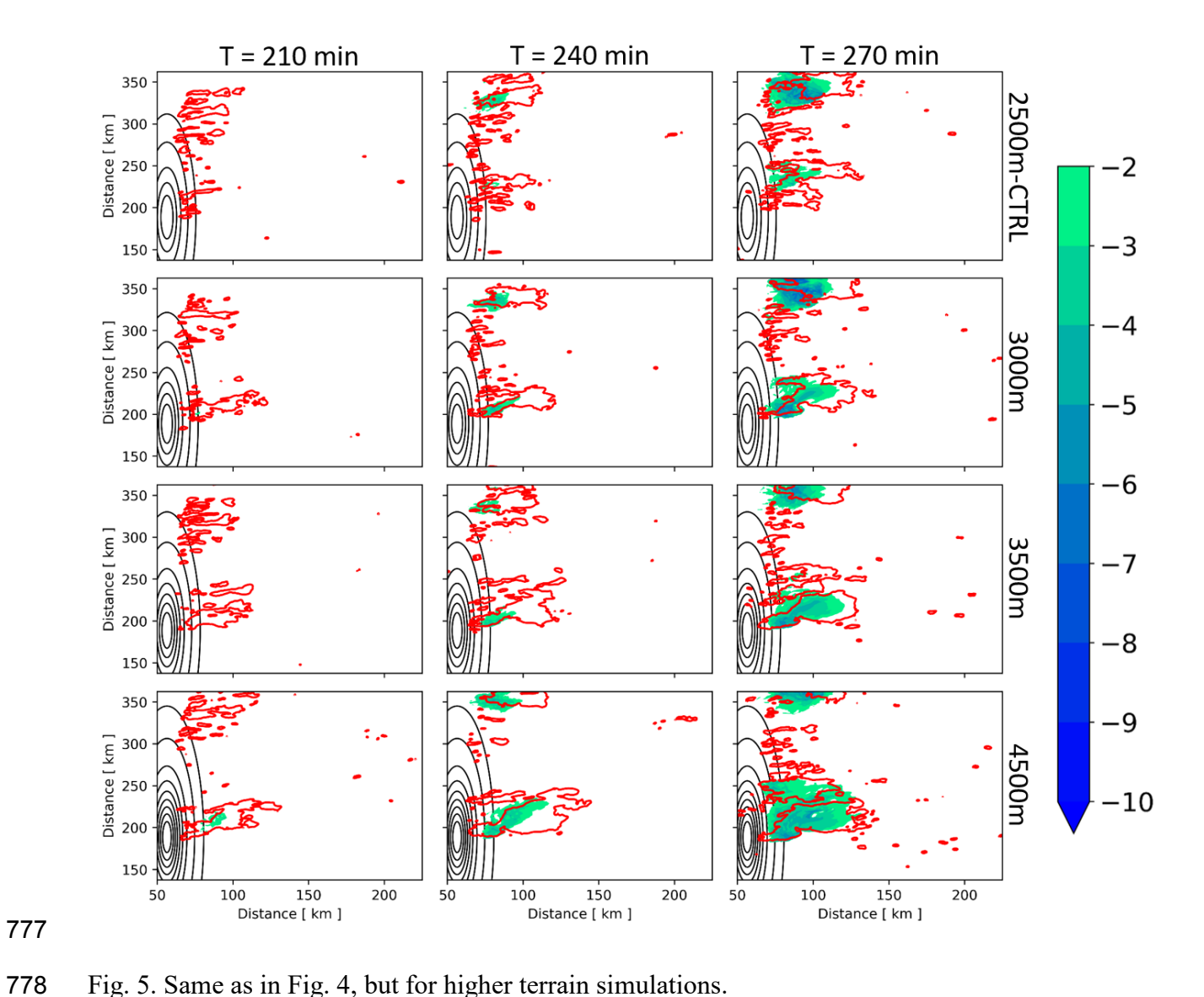


Fig. 5. Same as in Fig. 4, but for higher terrain simulations.

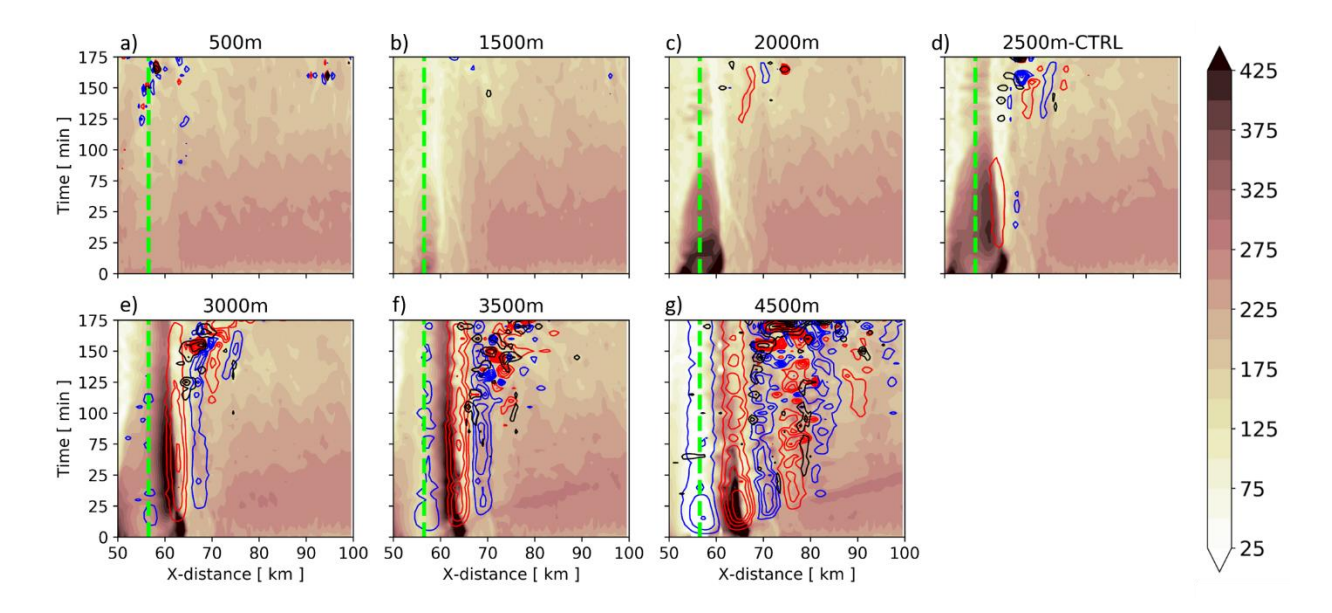


Fig. 6. West-to-east oriented Hovmöller diagrams of surface-based (positive) CIN (shaded; J kg⁻¹), vertical velocity (every 1 m s⁻¹ starting at +/- 1 m s⁻¹; reds = upward, blues = downward) and cloud water path (black contours every 1 kg m⁻², starting at 1 kg m⁻²) taken through the terrain peaks and calculated at 1000 m above the terrain peaks during the first 3 h of the simulations. The lime green dotted line denotes the location of the terrain peaks. Note that only a portion of the full domain is shown.

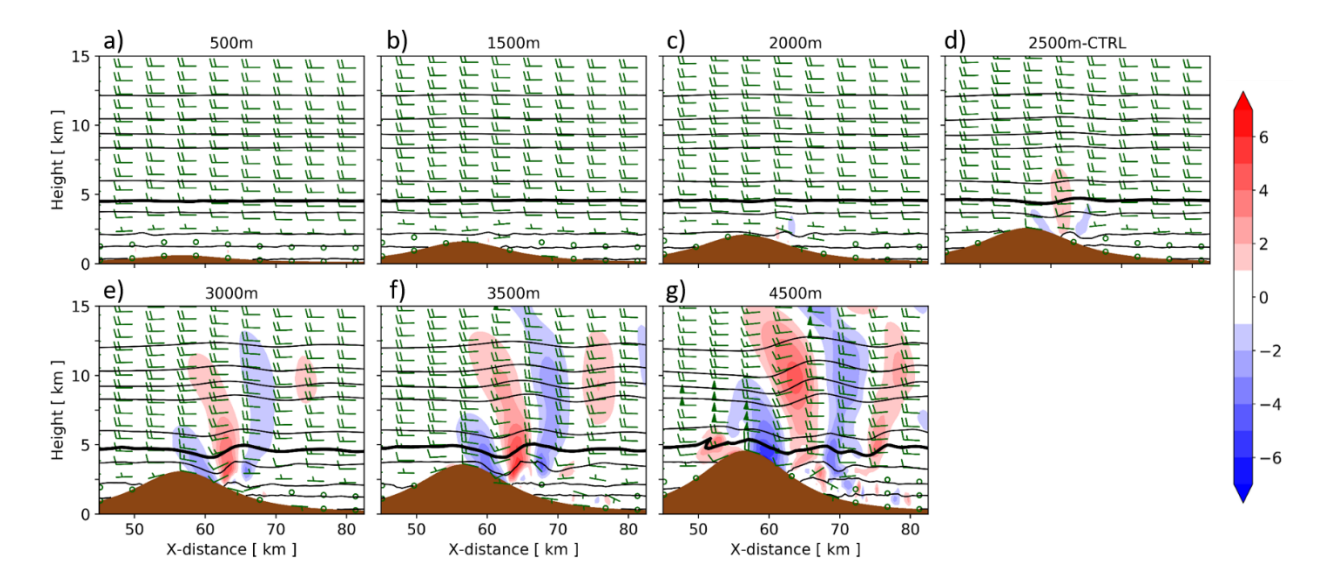


Fig. 7. West-to-east oriented vertical cross sections through terrain peaks (dark brown shading) of vertical velocity (shaded; m s⁻¹), potential temperature (contoured in black every 5 K; thick black reference line = 325 K), and in-plane winds (dark green barbs; half barb = 5 m s⁻¹; full barb = 10 m s⁻¹; pennant = 25 m s⁻¹) at 60 min into the simulations for (a) 500m, (b) 1500m, (c) 2000m, (d) 2500m-CTRL, (e) 3000m, (f) 3500m, and (g) 4500m terrain experiments. Note that only a portion of the full domain is shown.

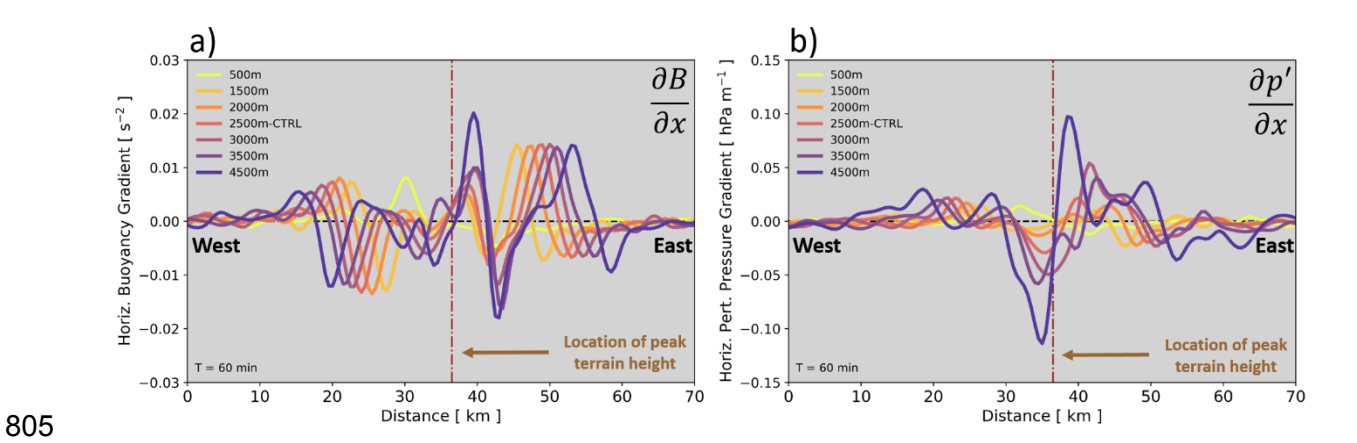


Fig. 8. West-to-east oriented cross sections of (a) horizontal buoyancy gradient (s⁻²) and (b) horizontal perturbation pressure gradient (hPa m⁻¹) at the lowest model level at 60 min into the simulations. The location of the peak terrain height is the vertical dot-dash brown line. Note that only a portion of the full domain is shown.

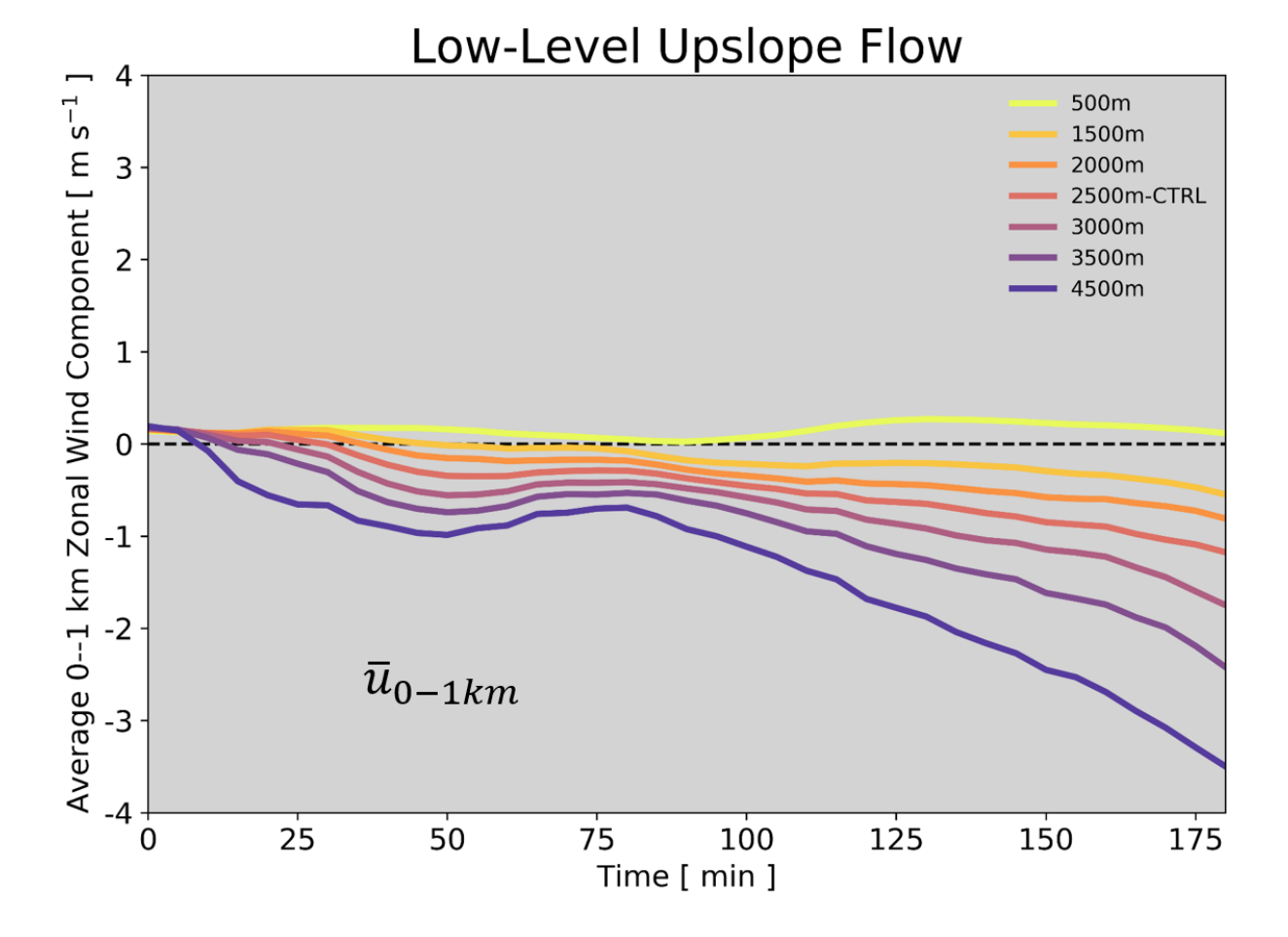


Fig. 9. Time series of vertically averaged 0-1 km zonal wind (m s⁻¹) that was spatially averaged over a 50×200 km² box with the west-central side of the box centered ~ 50 km east of terrain peaks for each simulation.

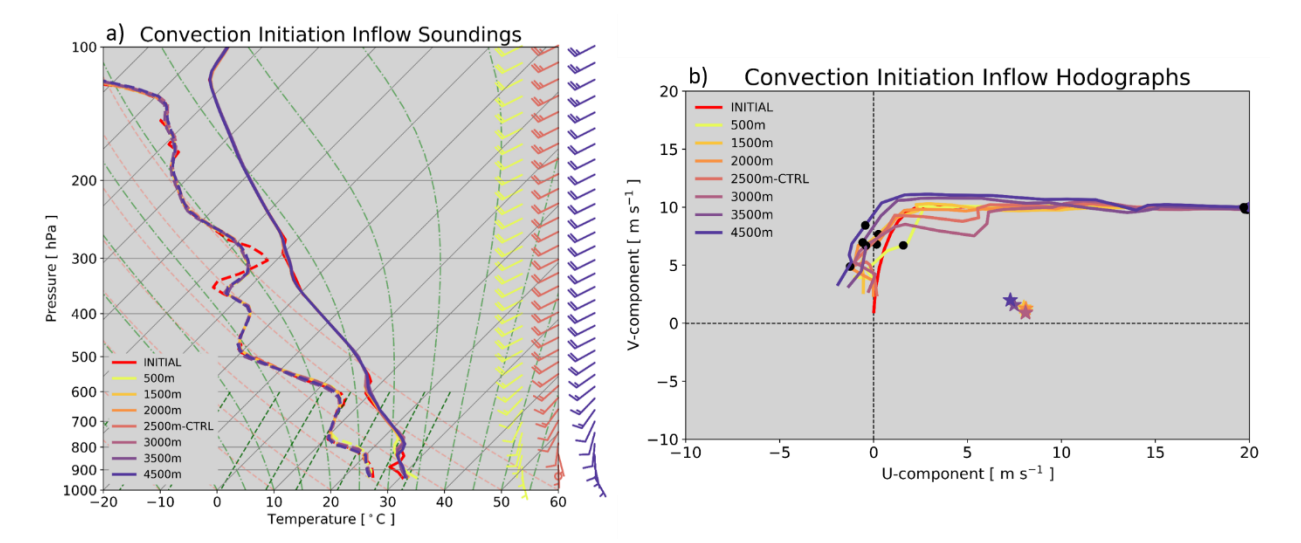


Fig. 10. Convection initiation soundings (taken 25 x 25 km² to the south and east of the first appearance of lowest model level reflectivity = 40 dBZ) plotted on a skew- $T \log P$ diagram (panel a). The rightmost solid lines are air temperatures (°C), the leftmost dashed lines are dewpoint temperatures (°C), and the 500 m (yellow), 2500m-CTRL (orange), and 4500 m (purple) terrain height simulation horizontal winds (half barb = 5 m s⁻¹; full barb = 10 m s⁻¹) are located on the right hand side of the sounding. Convection initiation vertical wind profiles plotted on a hodograph (panel b). The u-component of the wind is on the x-axis (m s⁻¹) and the v-component of the wind is on the y-axis (m s⁻¹). Colored stars denote the Bunkers right-moving supercell storm motion estimates (Bunkers et al. 2000). Black dots represent the horizontal wind at 1 and 6 km, respectively. The initial background state sounding and hodograph are shown in red.

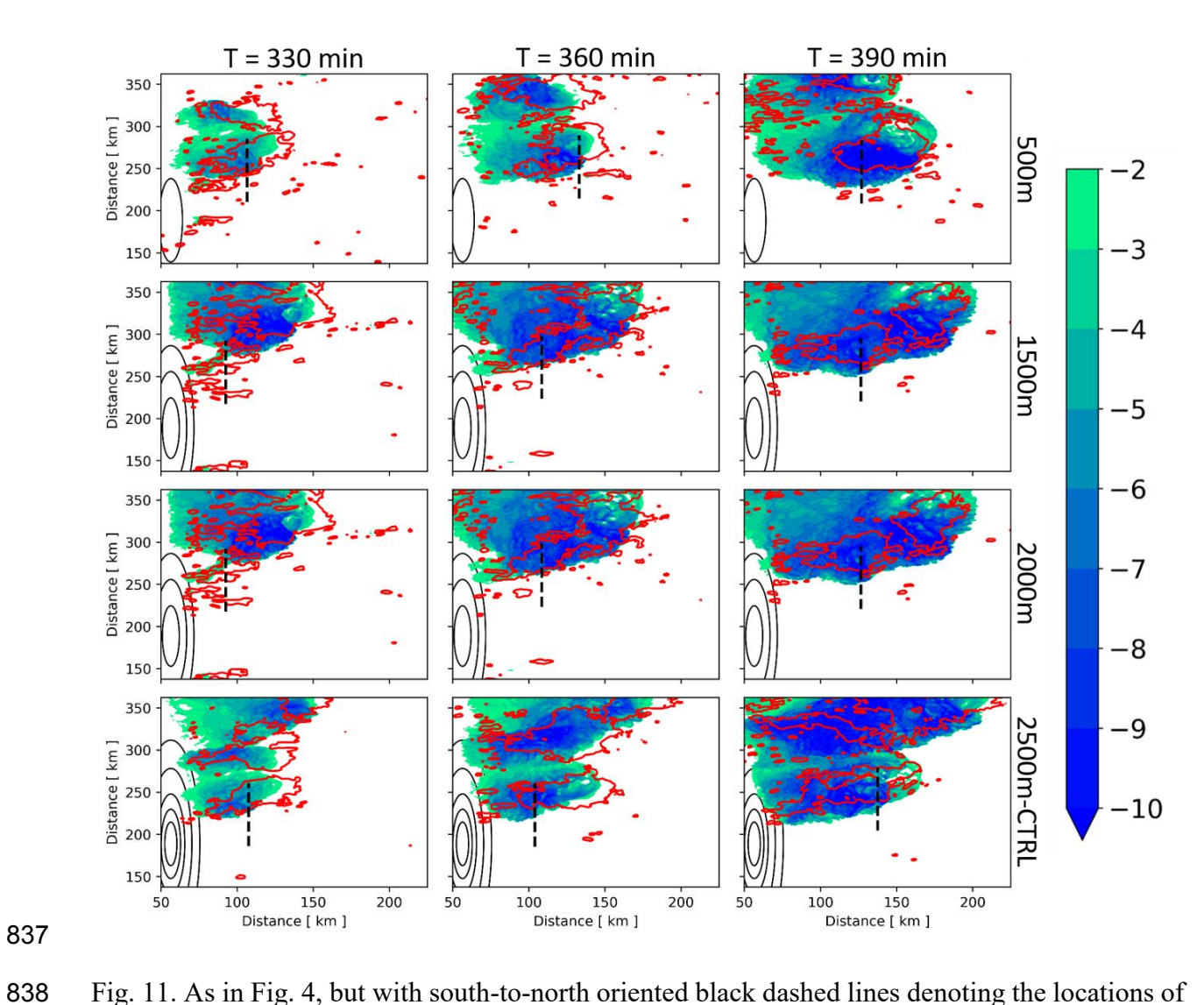


Fig. 11. As in Fig. 4, but with south-to-north oriented black dashed lines denoting the locations of where the vertical cross-sections in Fig. 13 are taken along.

839

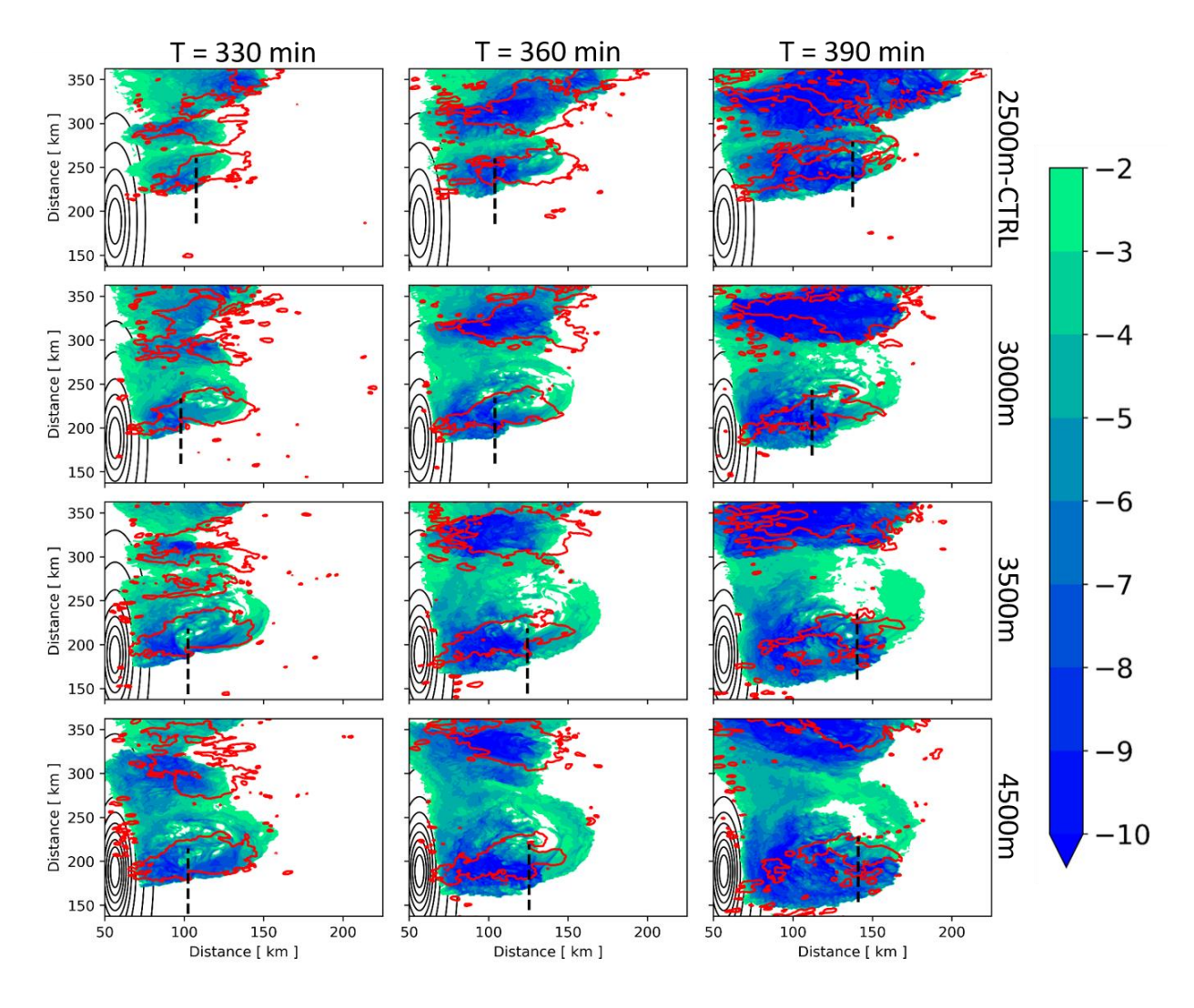


Fig. 12. Same as in Fig. 11, but for higher terrain simulations and with south-to-north oriented black dashed lines denoting the locations of where the vertical cross-sections in Fig. 14 are taken along.

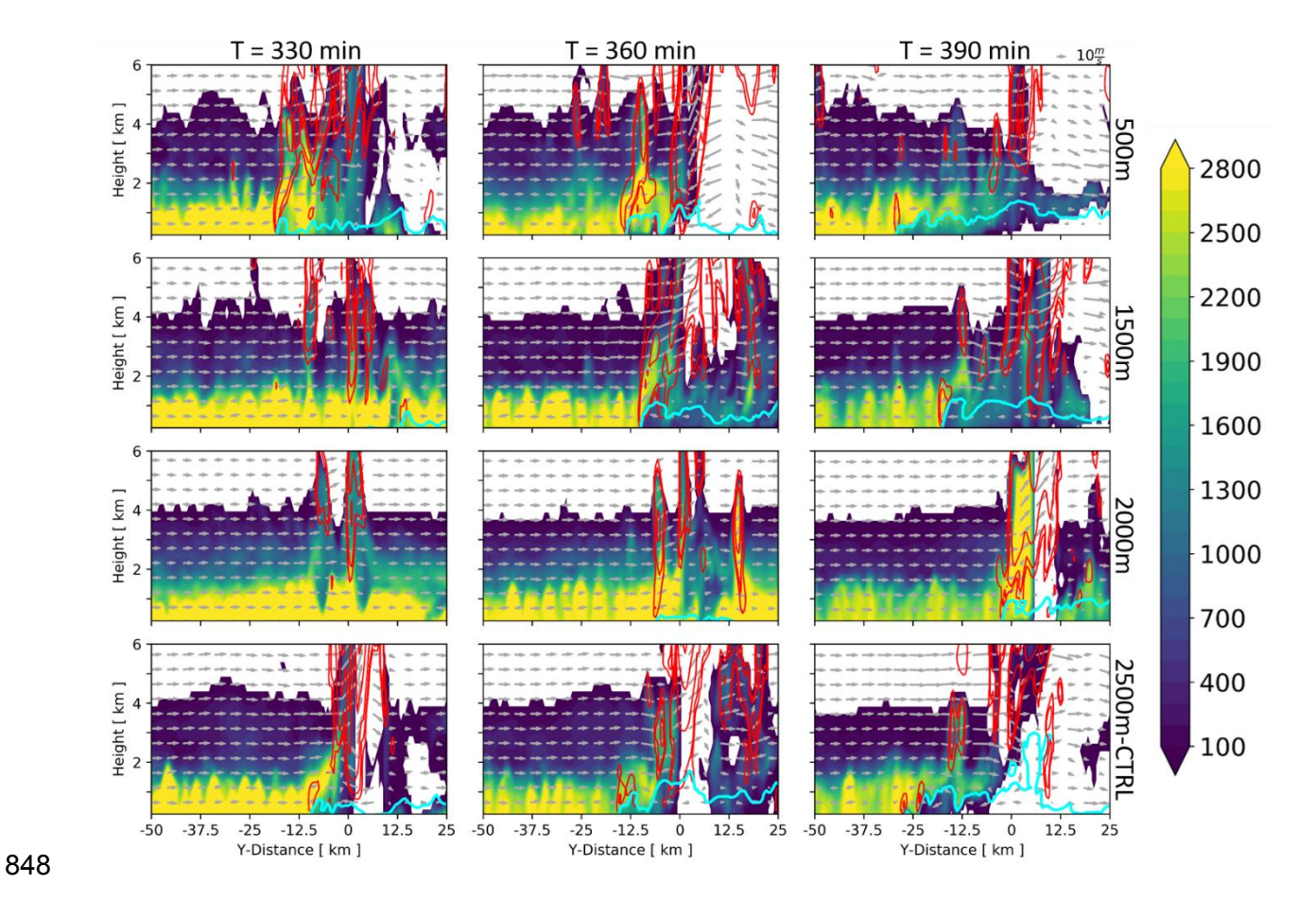


Fig. 13. South-to-north oriented vertical cross-sections taken through the black dashed lines in Fig. 11 depicting CAPE (shaded; J kg⁻¹) lifted from every grid point in cross section, potential temperature perturbation (cyan contour = -3 K), vertical velocity (red contours = 3, 5, 10, 20, 30, 40, 50, 60, 70, 80, and 90 m s⁻¹), and cross-section-parallel winds (grey vectors; legend at top right of figure). The location of UH_{MAX} is at Y-distance = 0 km, with south to the left (negative Y-distances) and north to the right (positive Y-distances). Rows = specific terrain simulation; Columns = output time (every 30 min). Note that only a portion of the full domain is shown.

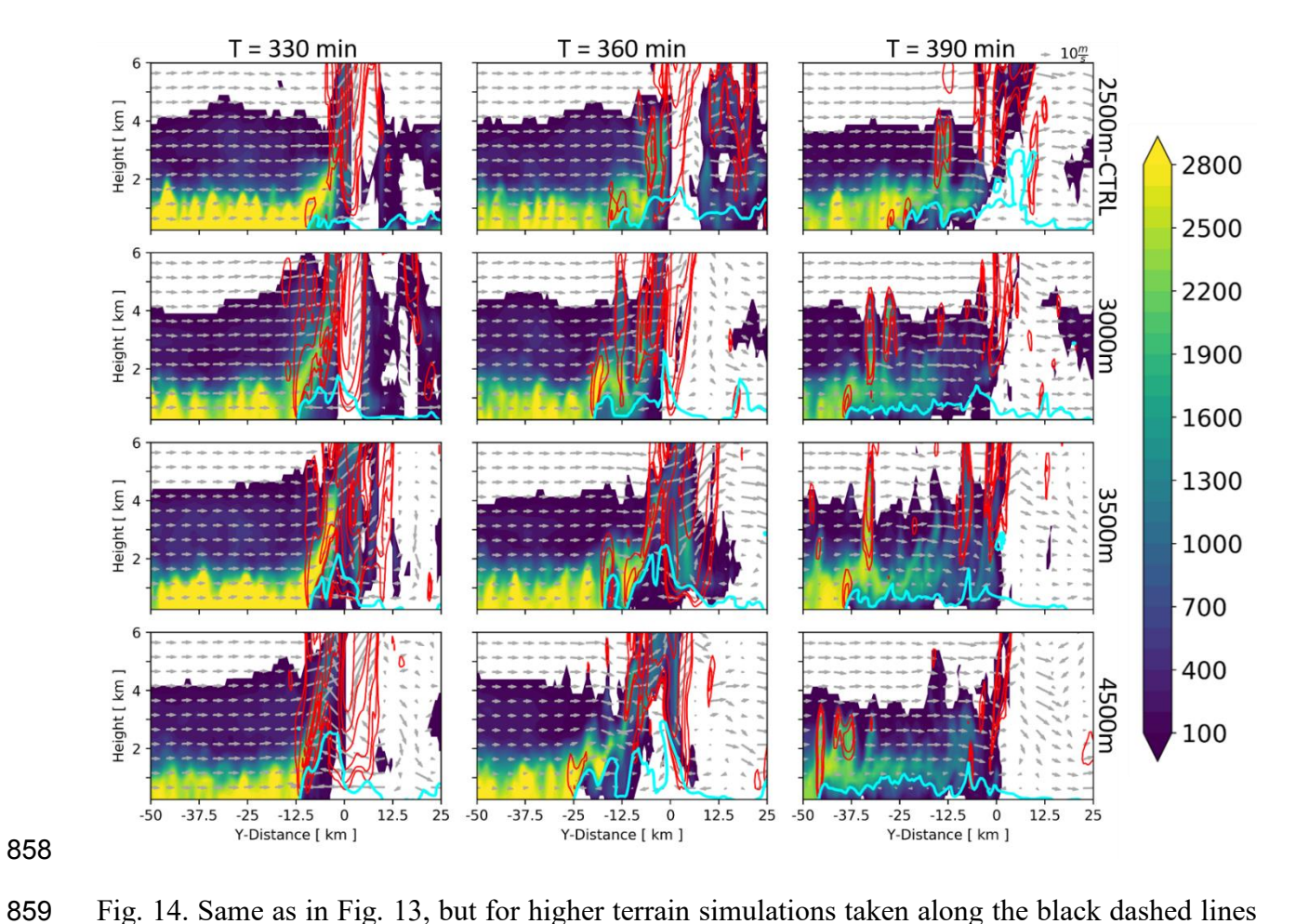


Fig. 14. Same as in Fig. 13, but for higher terrain simulations taken along the black dashed lines in Fig. 12.

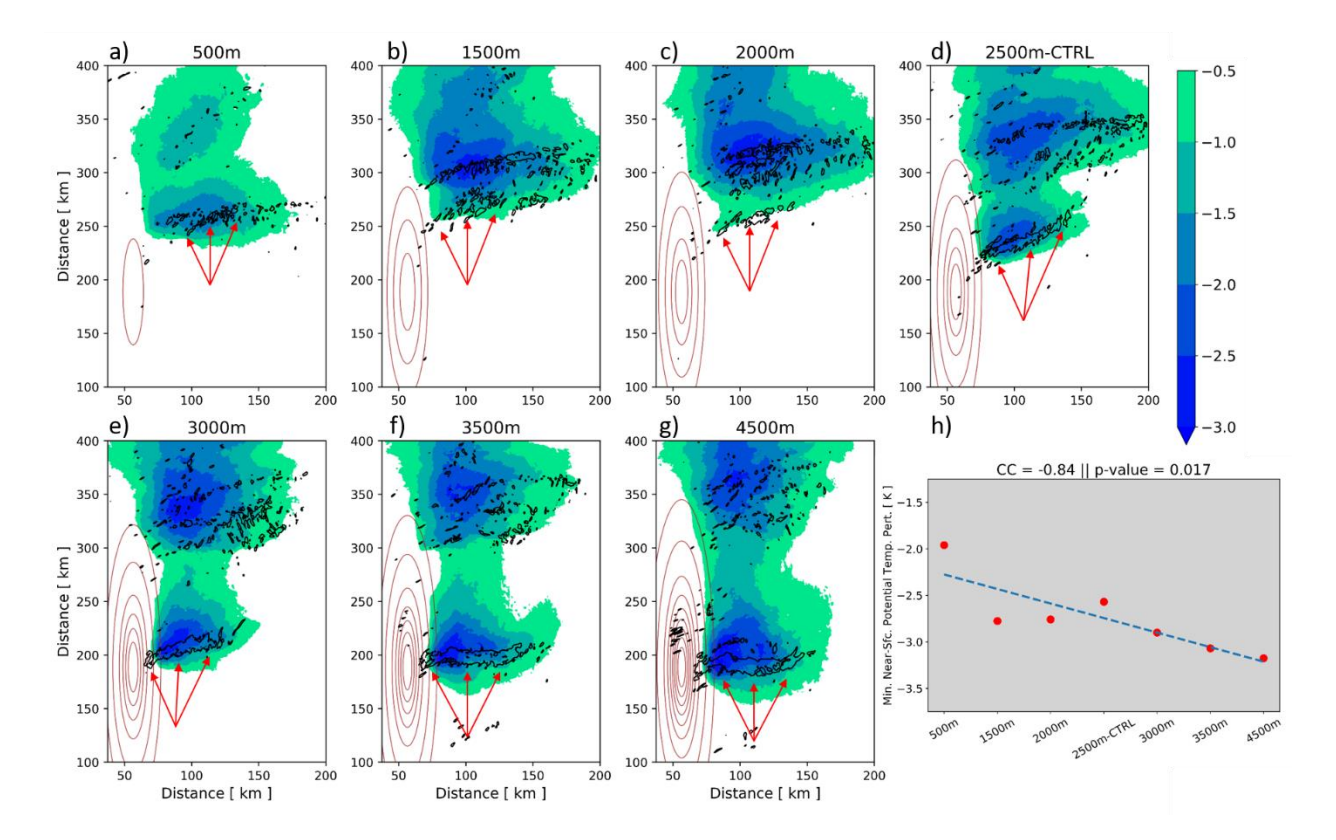


Fig. 15. Plan views (panels a-g) of lowest model level potential temperature perturbation averaged over the first 7 h of the simulations (shaded; K), accumulated 2–5 km UH swaths (black contour = $500 \text{ m}^2 \text{ s}^{-2}$), and terrain height (brown contours = 250 m, 500 m, and 500 m increments thereafter). In panel h: minimum lowest model level potential temperature perturbation averaged over the first 7 h of the simulations (K) (red dots; y-axis) vs. terrain height simulation (x-axis), best fit line (blue dashed line), and the CC and p-values (listed in the title above the plot). Note that only a portion of the full domain is shown in panels a-g. Note that the red arrows denote the track of the analyzed predominant right-moving supercell closest to the terrain.

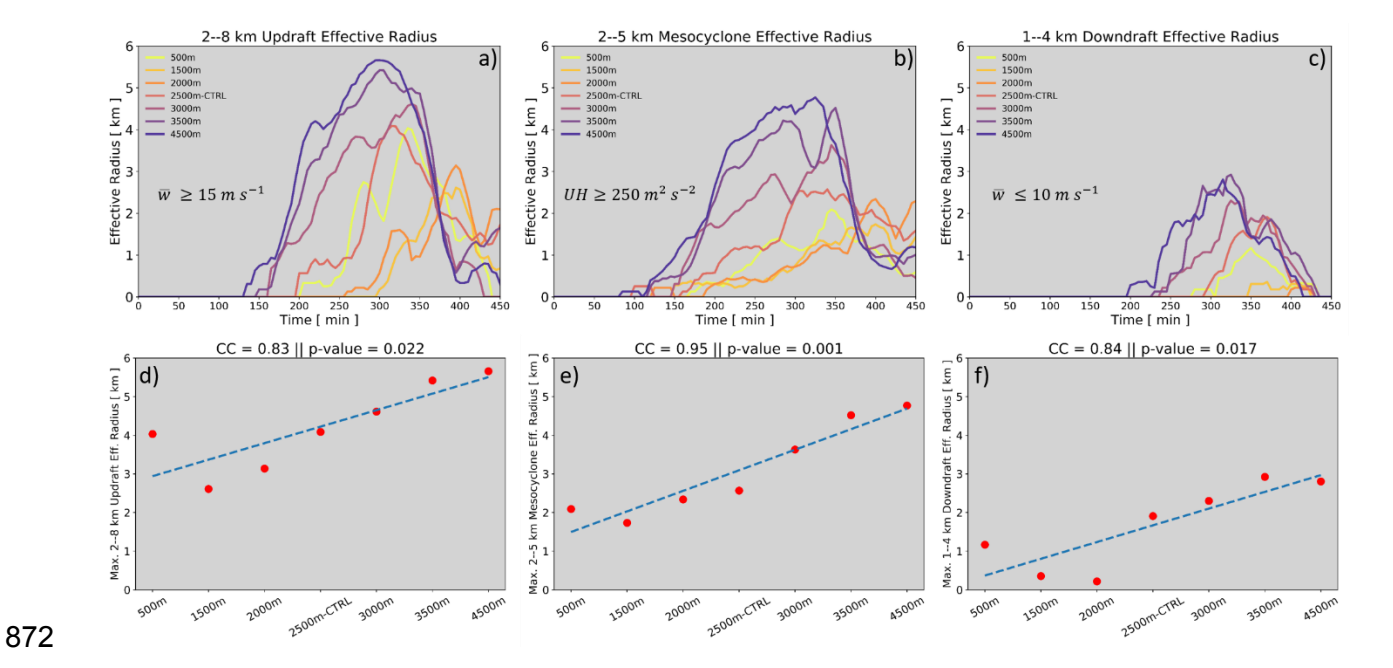


Fig. 16. Panels a-c: time series of (a) R_{up} (km), (b) R_{meso} (km), and (c) R_{dn} (km). Panels d-f: (d) maximum R_{up} (km) (red dots; y-axis) vs. terrain height simulation (x-axis), (e) maximum R_{meso} (km) (red dots; y-axis) vs. terrain height simulation (x-axis), and (f) maximum R_{dn} (km) (red dots; y-axis) vs. terrain height simulation (x-axis). In panels d-f, the best fit line is shown as a blue dashed line and the CC and p-values are listed in the title above each plot.

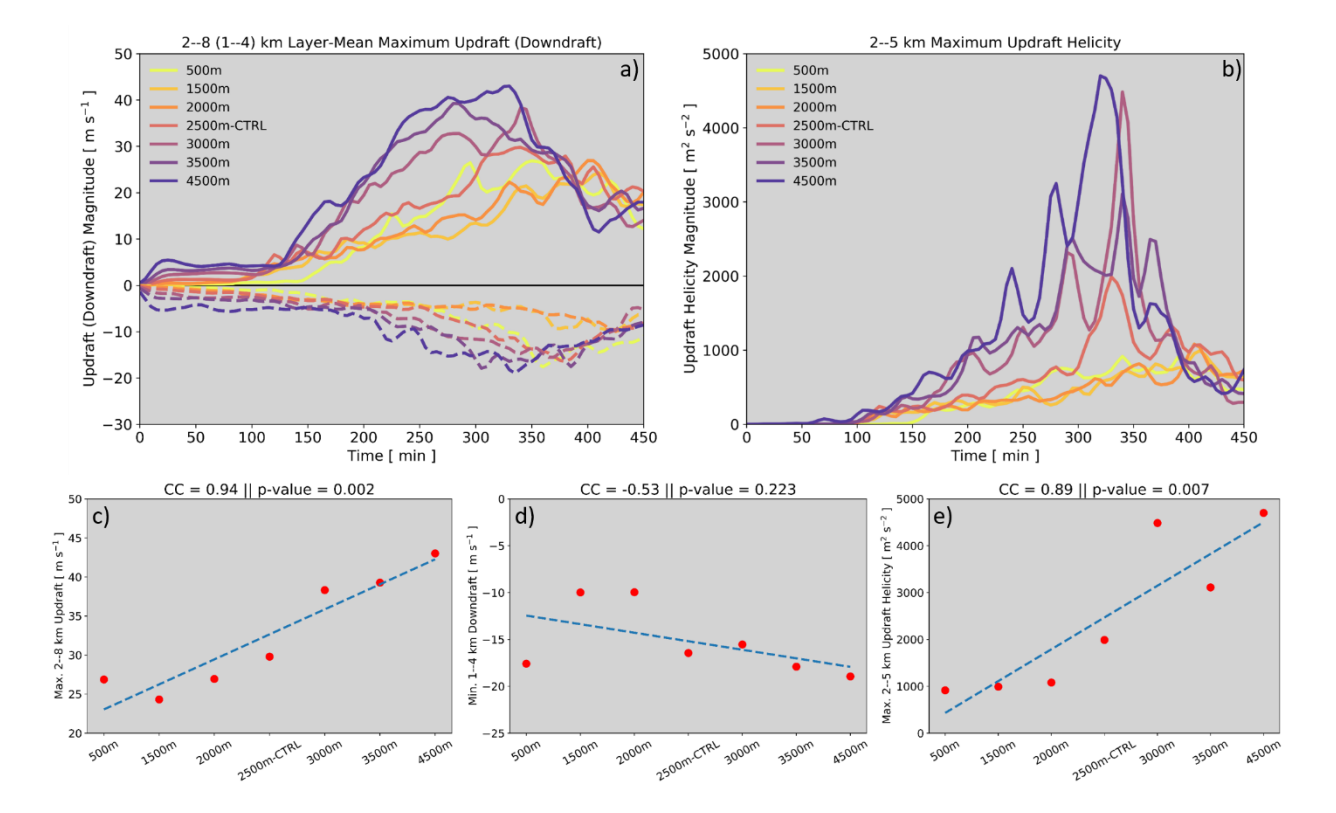


Fig. 17. Panels a-c: time series of (a) $\overline{w_{up}}$ (solid lines; m s⁻¹) and $\overline{w_{dn}}$ (dashed lines; m s⁻¹) and (b) UH_{MAX} (m² s⁻²). Panels c-e: (c) maximum $\overline{w_{up}}$ (m s⁻¹) (red dots; y-axis) vs. terrain height simulation (x-axis), (d) minimum $\overline{w_{dn}}$ (m s⁻¹) (red dots; y-axis) vs. terrain height simulation (x-axis), and (e) maximum UH_{MAX} (m² s⁻²) (red dots; y-axis) vs. terrain height simulation (x-axis). In panels c-e, the best fit line is shown as a blue dashed line and the CC and p-values are listed in the title above each plot.

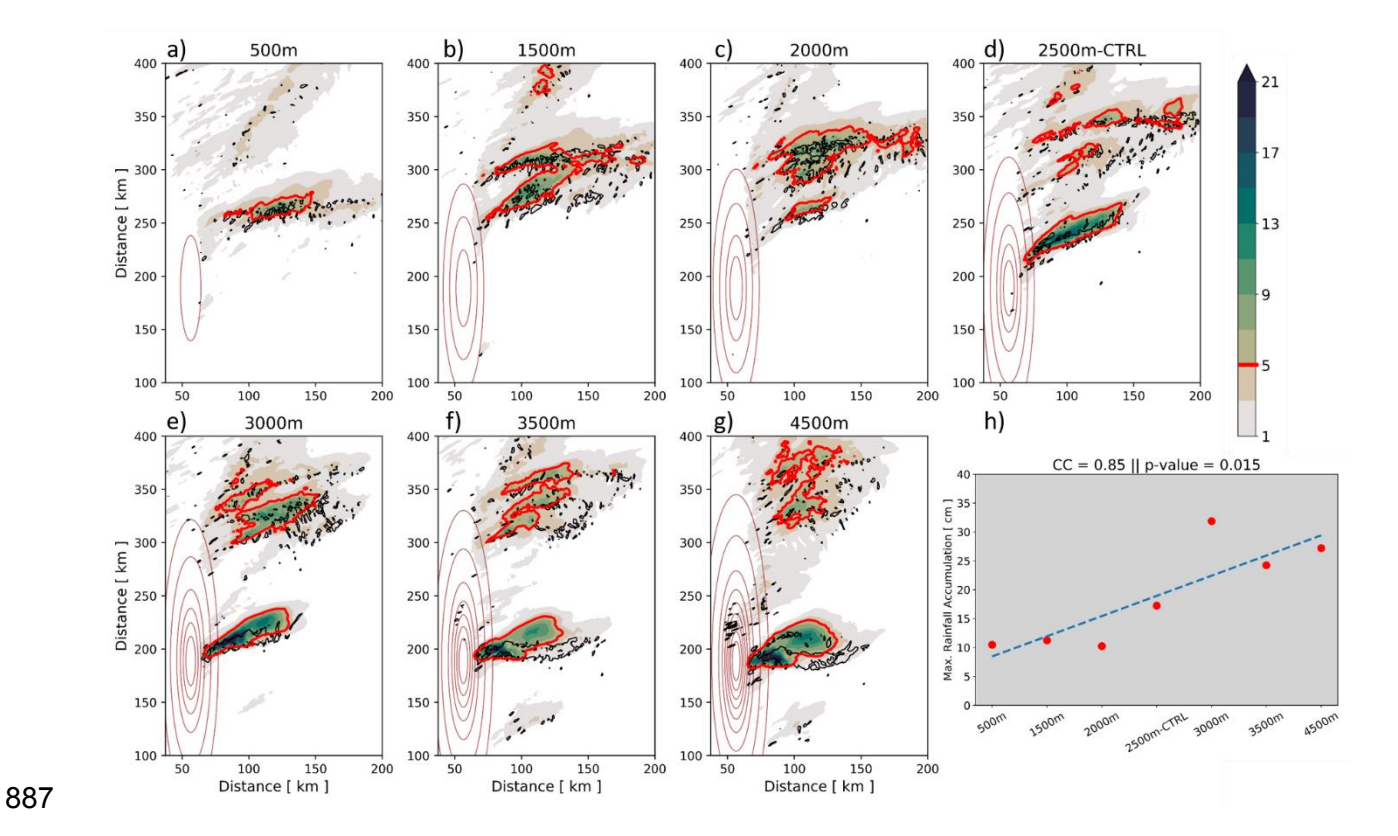


Fig. 18. Same as in Fig. 15, but runtime rainfall accumulation (shaded; cm) and the 5 cm runtime rainfall accumulation contour (red). As in Fig. 15, the black contour is accumulated 2–5 km UH swaths = $500 \text{ m}^2 \text{ s}^{-2}$. In panel h: maximum runtime rainfall accumulation (cm) (red dots; *y*-axis) vs. terrain height simulation (*x*-axis), best fit line (blue dashed line), and the *CC* and *p*-values (listed in the title above the plot).

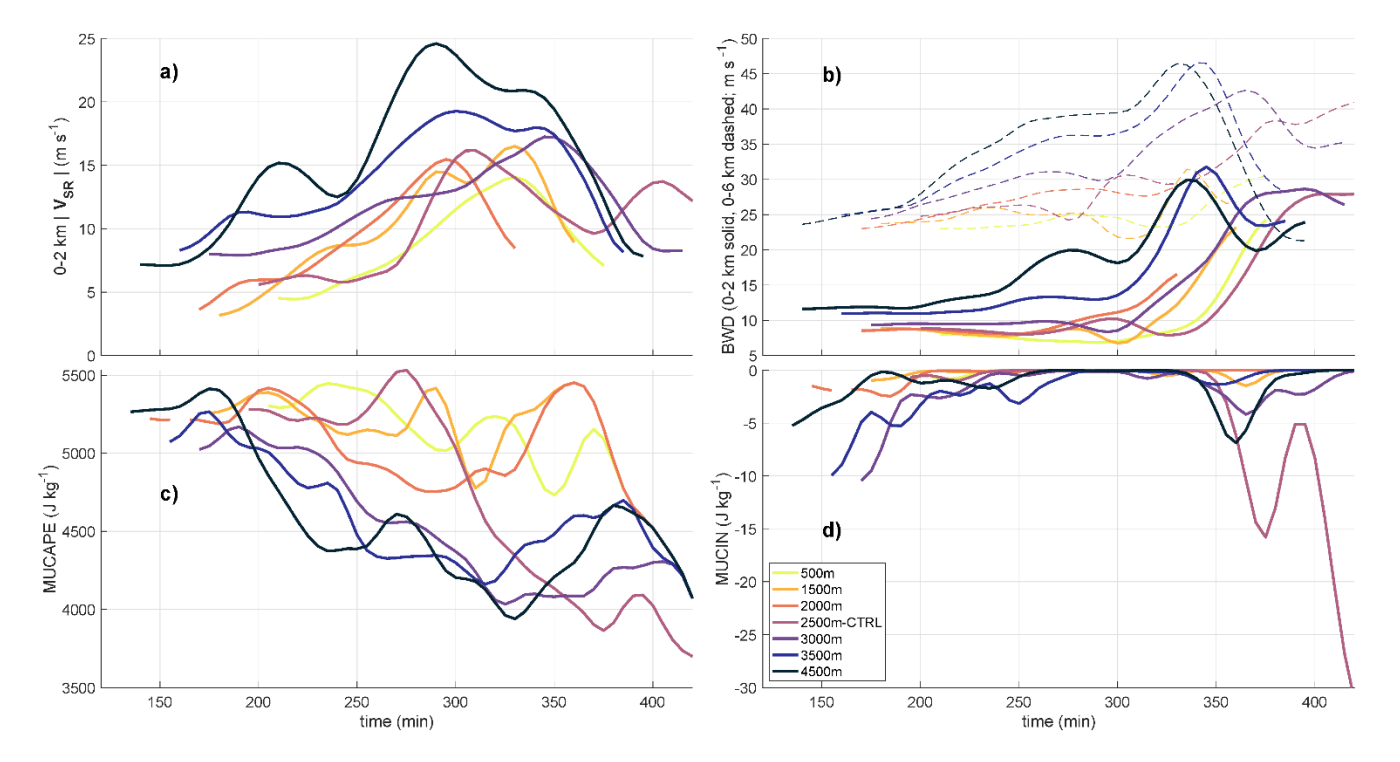


Fig. 19. Time series of quantities calculated within the supercell inflow box (calculation method described in text): (a) 0–2 km horizontal storm-relative (SR) flow magnitude (m s⁻¹), (b) 0–2 (solid lines) and 0–6 (dashed lines) km bulk wind difference magnitude (BWD; m s⁻¹), (c) most-unstable CAPE (MUCAPE; J kg⁻¹), and (d) most-unstable CIN (MUCIN; J kg⁻¹). The legend for each terrain height simulation is located in panel d.

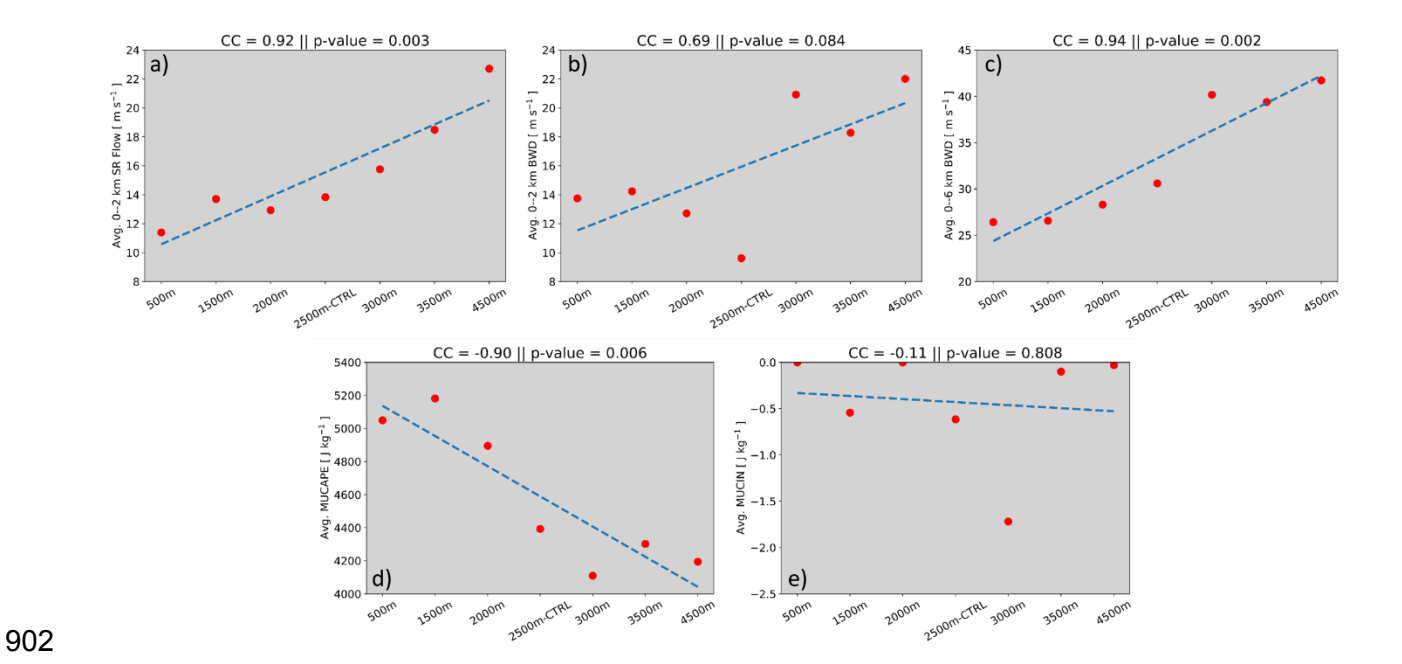


Fig. 20. Regression plots of: (a) average 0–2 km horizontal storm-relative (SR) flow magnitude (m s⁻¹) (red dots; *y*-axis) vs. terrain height simulation (*x*-axis), (b) average 0–2 km bulk wind difference magnitude (BWD; m s⁻¹) (red dots; *y*-axis) vs. terrain height simulation (*x*-axis), (c) average 0–6 km bulk wind difference magnitude (BWD; m s⁻¹) (red dots; *y*-axis) vs. terrain height simulation (*x*-axis), (d) average most-unstable CAPE (MUCAPE; J kg⁻¹) (red dots; *y*-axis) vs. terrain height simulation (*x*-axis), and (e) average most-unstable CIN (MUCIN; J kg⁻¹) (red dots; *y*-axis) vs. terrain height simulation (*x*-axis). The best fit line is shown as a blue dashed line and the *CC* and *p*-values are listed in the title above each plot.

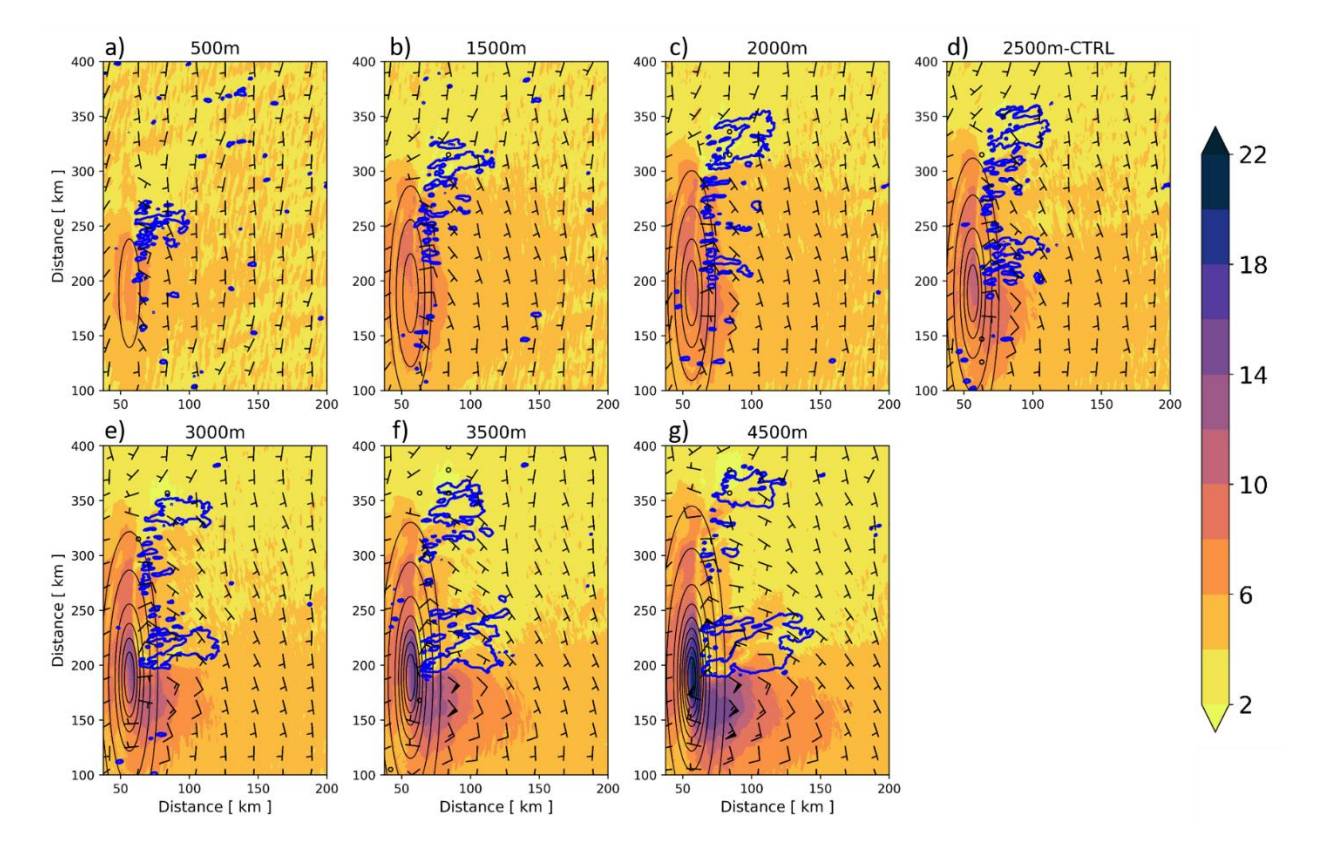


Fig. 21. Plan view plots of lowest model level horizontal perturbation winds (calculation method described in text; shaded = magnitude; half barb = 2 m s^{-1} ; full barb = 4 m s^{-1} ; pennant = 6 m s^{-1}), lowest model level reflectivity at 4 h into simulations (blue contour = 40 dBZ), and terrain height (black contours = 250 m, 500 m, and 500 m increments thereafter). Note that only a portion of the full domain is shown.